university of groningen / faculty of science and engineering

INTEGRATION OF CHIRAL MECHANICAL METAMATERIALS IN SOFT ROBOTIC GRIPPERS FOR AGRICULTURAL HARVESTING

Tijn van Nieuwenhuyzen
S5405394

Computational Mechanical and Materials Engineering group (ENTEG)

January 16th, 2026

Bachelor's Thesis

1st Supervisor: Prof. dr. Anastasiia Krushynska, Computational Mechanical and Materials Engineering, ENTEG, Faculty of Science and Engineering, University of Groningen

2nd Supervisor: Ioannis Spanos, Computational Mechanical and Materials Engineering, ENTEG, Bio-inspired MEMS and Biomedical Devices, Faculty of Science and Engineering, University of Groningen

Abstract

Soft robotic grippers have great potential for handling delicate agricultural products, but a key challenge lies in balancing mechanical softness for gentle interaction with sufficient structural stiffness to enable stable and reliable grasping. This thesis investigates the integration of a chiral mechanical metamaterial into a soft robotic gripper to convert axial deformation into controlled rotational motion and assess its effect on rotation transfer and contact behavior. Finite element simulations were performed to analyze the rotational response of the gripper and the resulting contact behavior between the gripper and a grasped object. The results show that axial loading of the chiral structure is converted into controlled rotational motion of the gripper, which can be effectively transferred to a grasped object. Frictional contact enables the transfer of rotational motion, while comparing frictional and frictionless contact conditions shows that friction has a limited influence on the contact behavior during twisting of deformable objects. These findings demonstrate the potential of chiral mechanical metamaterials to enhance soft robotic grippers with combined grasping and twisting capabilities for agricultural harvesting applications.

Contents

1 Introduction

Soft robotic grippers have emerged as an effective solution to automate the harvesting process of delicate objects, such as tomatoes. They enable the gentle picking of fruits and vegetables, which can reduce damage and help address the decreasing availability and high demand for manual labor [1]. Their flexible and adaptive structures make them particularly suitable for handling irregularly shaped and delicate items, which traditional rigid grippers struggle to manage efficiently [2]. Despite the potential of soft grippers, large-scale agricultural adoption remains limited. A key challenge in the design of soft robotic systems is finding a balance between mechanical softness and structural strength. On the one hand, grippers need to be soft enough to prevent damage when interacting with delicate objects, while on the other hand, they must be stiff and strong enough to ensure stable and reliable grasping [3]. In the context of agricultural harvesting, this balance is crucial for enabling gentle yet secure handling of products.

A promising approach to further enhance the capabilities of soft robotic grippers is the integration of metamaterials. These engineered materials have unusual mechanical properties, which arise from the material's structure rather than its composition [4]. The structure of mechanical metamaterials enables functionalities such as negative Poisson's ratios and programmable stiffness [5]. The integration of mechanical metamaterials into soft grippers can enhance their adaptability and stability, which allows them to better conform to diverse object shapes while providing gentle yet secure handling [6]. Additionally, the structural design of metamaterials can help distribute contact forces more evenly and reduce the overall weight, which enhances efficiency and ease of movement.

An interesting class of mechanical metamaterials is chiral mechanical metamaterials. These materials have an asymmetric internal geometry that cannot be mirrored. Because of this asymmetry, compressing the structure can cause it to twist, instead of only shortening along the direction of the applied load [7]. The internal twisting deformation of the chiral metamaterial can be transferred as a rotational motion to the structure it is attached to [8]. For a soft robotic gripper, this would enable the gripper fingers to rotate around the object during gripping. Such rotation could improve the ease of securing the object and enhance contact stability. However, to the best of the author's knowledge, there is currently no research addressing the integration of chiral metamaterials into soft robotic grippers for the purpose of generating a controlled rotational motion of the gripper and the grasped object.

The objective of this project is to study how rotational deformation from a chiral mechanical metamaterial can be transferred to a soft gripper and a grasped object. The thesis focuses on quantifying the rotation of the gripper and the grasped object caused by axial loading of the chiral structure. In addition, it examines how this rotation affects the contact behavior between the gripper and the object. Therefore, the central research question of this thesis is: What is the effect of integrating a chiral mechanical metamaterial into a soft robotic gripper on the transfer of rotational deformation and the resulting contact behavior?

This thesis is structured as follows. Section 2 reviews relevant literature on soft robotic grippers and mechanical metamaterials. Section 3 describes the modeling and simulation methods used in this thesis. Section 4 presents and analyzes the simulation results. Finally, Sections 5 and 6 discuss the results and summarize the main conclusions of the research.

2 Literature Review

2.1 Soft Robotic Grippers

Traditional robots consist of rigid joints connected through links, which are each actuated by electric motors. In contrast, soft robots generate motion through the deformation of soft materials [9]. Their actuation is mainly achieved using pneumatic drive, hydraulic drive, cable-driven mechanisms, and electrical drive. Traditional robotic grippers face significant limitations in agricultural harvesting due to their use of stiff materials and rigid links. This limits them in tasks such as handling fragile objects and grasping irregularly shaped items. Soft robotic grippers use highly elastic and extensible materials, such as shape memory alloys and dielectric elastomers. These materials are highly flexible, making soft robotic grippers a promising solution for tasks that traditional robotic grippers struggle with [10].

Several soft robotic grippers for the harvesting of delicate objects already exist. Most studies focus on the harvesting of one object at a time. One of the most widely used designs is the pneumatic bending gripper [9]. In the work of Kultongkham et al [11], for example, a pneumatic soft gripper is used for the harvesting of tomatoes, as shown in Figure 1a. This soft gripper consists of three gripper fingers, which operate together through a pneumatic control system. When the gripper is actuated, air inside the chamber is pressurized, allowing the fingers to bend around the tomato.

Another common actuation strategy for soft grippers is the tendon-driven mechanism. In tendon-driven soft grippers, movement is created by pulling cables embedded in the soft structure, which are typically driven by electric motors. This mechanism allows the gripper fingers to bend in a controlled manner and adapt to the shape and size of the object. According to Liu et al. [12], tendon-driven soft grippers can apply different levels of grasping force while still keeping a soft contact with the object, which makes them suitable for handling delicate agricultural products. An example of a tendon-driven gripper is shown in Figure 1b, taken from the study by Gunderman et al. [13]. The study presents a new tendon-driven gripper designed for harvesting delicate objects, as well as for handling objects used in daily activities.

Although soft grippers offer advantages for handling delicate objects, their adoption in practical agricultural applications remains limited. This is mainly due to challenges soft grippers face, such as limited robustness and durability of soft materials, relatively weaker output force compared to rigid grippers [12], and the need for more advanced actuation systems and cost-effective manufacturing methods [14].

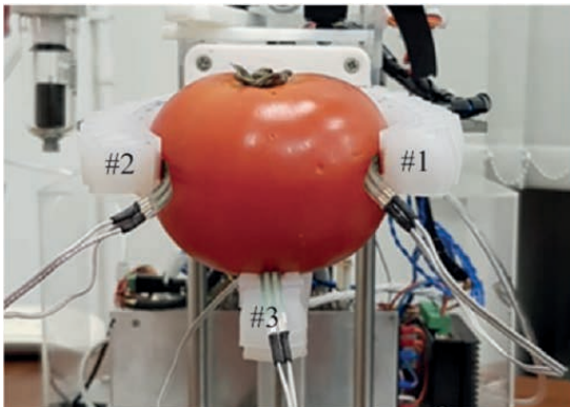

(a) Pneumatic soft gripper [11].

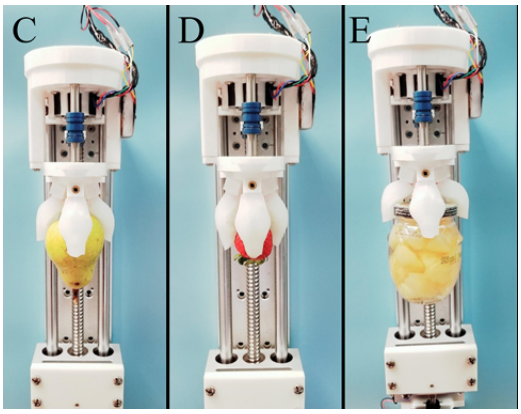

(b) Tendon-driven soft gripper [13].

Figure 1: Examples of soft robotic grippers used in agricultural harvesting.

2.2 Mechanical Metamaterials

Metamaterials are engineered materials whose effective properties arise from their internal structure rather than from their chemical composition [4]. By designing the shape, size, and arrangement of repeating unit cells, the material response can be programmed to achieve specific properties [15]. These properties and functionalities are impossible or difficult to achieve with conventional materials. A specific group of metamaterials that is especially relevant for the harvesting of delicate objects is mechanical metamaterials, which enable tailored mechanical responses such as reprogrammable stiffness, complex deformation modes, and guided motion [4]. This level of control over the mechanical response makes mechanical metamaterials suitable for applications involving interactions with delicate objects.

Mechanical metamaterials can exhibit a wide range of unconventional mechanical behaviors as a result of their internal structure. These behaviors have been widely studied in the literature, and some examples are auxetic metamaterials with a negative Poisson's ratio, metamaterials with vanishing shear modulus, metamaterials with negative compressibility, singularly nonlinear materials, and topological metamaterials [16]. Auxetic metamaterials are the most widely studied class of mechanical metamaterials. They exhibit a negative Poisson's ratio, meaning that they expand sideways when stretched and contract sideways when compressed. The most common type of auxetic metamaterials is based on re-entrant structures, which are defined by inward-oriented cell ribs with negative internal angles. An example of such a re-entrant geometry is the re-entrant honeycomb structure presented by Kolken et al. [17], which illustrates the characteristic deformation mechanism of auxetic metamaterials, as shown in Figure 2.

When auxetic metamaterials come into contact with an object, their deformation behavior can enable improved conformability as the structure adapts to the shape of the object. This improved conformability allows contact forces to be distributed more evenly, reducing local stress concentrations. Such behavior is advantageous for applications involving the interaction with delicate objects.

Despite the advantages of the deformation behavior of auxetic metamaterials, their response is primarily characterized by symmetric expansion or contraction. In this thesis, the objective is to achieve an additional functionality in the form of controlled rotational motion. Therefore, the focus is shifted to another subclass of mechanical metamaterials, namely chiral metamaterials, which are capable of converting translational deformation into rotational motion through their geometric asymmetry.

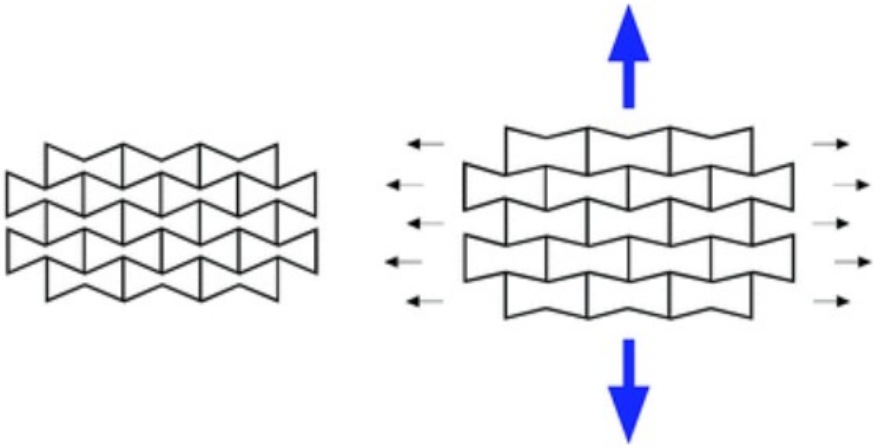

Figure 2: Re-entrant honeycomb structure. Left: Undeformed configuration. Right: Deformed configuration under tensile loading in the y-direction [17].

2.3 Chiral Mechanical Metamaterials

The term chirality was introduced by Lord Kelvin in 1894, when he defined a chiral object as one whose mirror image, even when it is ideally reflected, cannot be made to match the original [18, 19]. According to Wu et al, chiral mechanical materials are structures composed of chiral elements, which deform through node rotation and ligament bending. Due to their asymmetric structure, axial loading causes the rotating nodes and bending ligaments to combine into a twisting motion [19]. In their study, various 2D and 3D chiral unit cells were presented. In Figure 3, a selection of existing 3D chiral unit cells is shown to illustrate the wide variety of geometries.

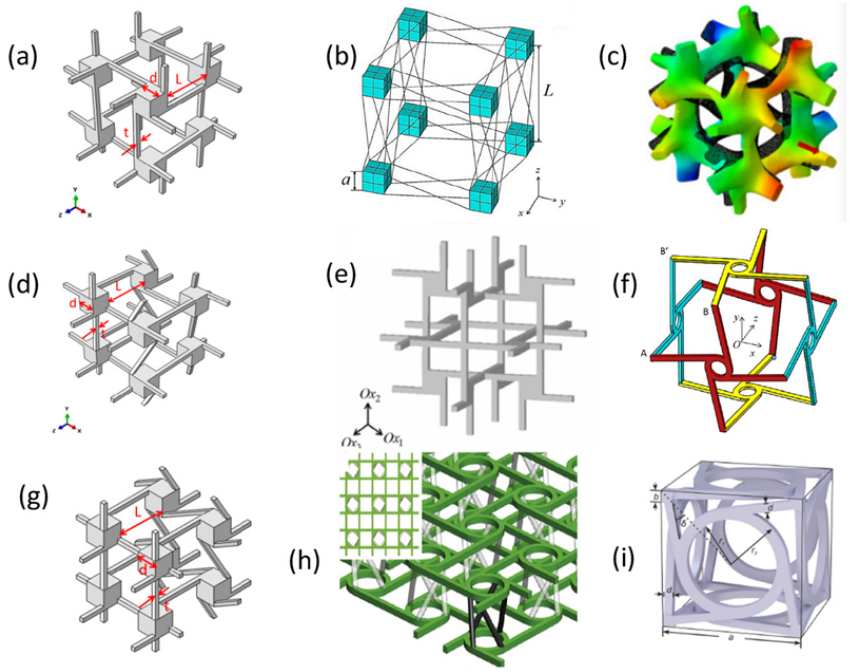

Figure 3: Examples of various 3D unit cells [19].

The amount of twist generated by a chiral unit cell is not fixed, but it depends on its geometric parameters. A Bachelor's Integration Project at the University of Groningen explored this dependency, revealing that variations in geometric parameters resulted in significant changes to the twisting response of the unit cell [20]. This project used a unit cell from a study by Frenzel et al. [21, 22] to show how different parameters affect the amount of twist of the chiral unit cell. The results showed that increasing the inner ring radius and the arm angle increased the twist angle of the unit cell. In contrast, increasing the thickness of the structure, the ring thickness, and the arm thickness resulted in a stiffer structure with a lower twist angle. In particular, the arm thickness had the most significant impact, as thinner arms allowed for more rotation and therefore a greater twist angle. This project showed that certain geometric parameters lead to significant twisting of the chiral unit cell. Since Frenzel et al. already provide an optimized chiral unit cell design that maximizes the twist response, their geometry was used in this thesis. The design of their chiral unit cell is therefore described in the following section.

Frenzel et al. conducted their research on microscale chiral unit cells [22]. However, the geometry is scale-independent and can therefore be applied at the macroscale in this thesis. In their design, the parameters were expressed relative to the lattice constant a, as shown in Table 1. This lattice constant determines the spacing between cells in the periodic structure and is defined using the in-plane con-

stants a_x and a_y. The physical dimensions of the chiral unit cell itself correspond to a cubic region of size $a_z \times a_z \times a_z$, with $a_z = \frac{2}{3}a_x = \frac{2}{3}a_y$. Thus, the lattice constant a acts as the reference length that defines the geometry of the chiral unit cell, as shown in Figure 4. In this thesis, the geometric parameters were also expressed relative to a, while a_z was used to describe the physical size of a single unit cell.

Table 1: Geometric parameters of the chiral unit cell by Frenzel et al.[22].

Parameter	**Value**
Outer ring radius (r_1)	$0.267\,a$
Inner ring radius (r_2)	$0.213\,a$
Arm/strut thickness (d)	$0.4\,a$
Arm angle (δ)	$34.8°$

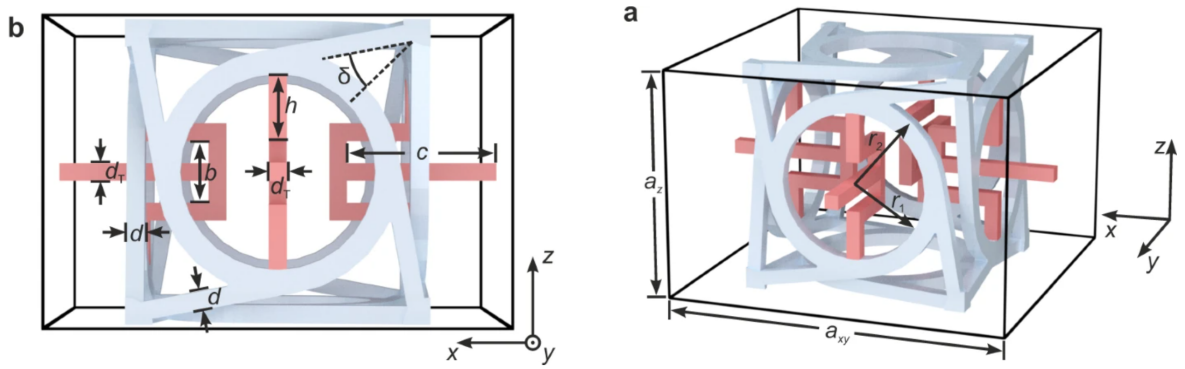

(a) 2D view of the chiral unit cell, showing the geometric parameters.

(b) 3D view of the chiral unit cell, showing the lattice constants.

Figure 4: 2D and 3D view of the chiral unit cell by Frenzel et al. [22].

Frenzel et al. showed in another study that for $N = 1$ the maximum twist response exceeded $2°/\%$ axial strain [21]. Here, the parameter N is defined as $N = \frac{L}{a}$, where L is the height of the sample and a the lattice constant. The total number of unit cells for their test sample was given by $(N \times N \times 2N) \times 2$, because a left-handed and right-handed pair was created to eliminate the net rotation in the experiments. These findings were taken into account for selecting the number of unit cells for the chiral column used in this thesis.

2.4 Mechanical Metamaterials Integrated in Soft Grippers

Several studies have investigated the integration of mechanical metamaterials in soft grippers to improve their functionality and adaptability. Many of these soft grippers are designed for agricultural harvesting applications, particularly for the handling of delicate fruits such as tomatoes. The geometry and dimensions of the designs in these studies are based on the size of the target crop to ensure gentle and reliable handling. In this thesis, the same approach is used, in which the gripper is designed

based on a medium-sized tomato with a diameter of 55 mm. This value corresponds to the medium-size category defined by Igno et al., who classify tomatoes according to agricultural standards into small (38–52 mm), medium (51–60 mm), and large (59–71 mm) size ranges [23].

Ansari et al. presented a soft gripper design integrated with auxetic metamaterials for the harvesting of tomato-like soft fruits [24]. In their design, a honeycomb auxetic meta-structure is integrated into the fingers of the gripper to improve compliance and adaptability during grasping. The study shows how the meta-structure deforms during grasping, allowing the gripper fingers to adapt to the shape of the tomato, as illustrated in Figure 5a.

Another example of a soft gripper integrated with metamaterials is presented by Tawk et al., as shown in Figure 5b. In their study, a soft gripper with pneumatic fingers was developed, in which a compliant mechanical metamaterial is integrated to improve conformal grasping of objects [6]. They showed that the integrated mechanical metamaterial, composed of an auxetic structure and compliant ribs, improved the conformability of the gripper fingers by increasing the contact area and reducing the contact pressure.

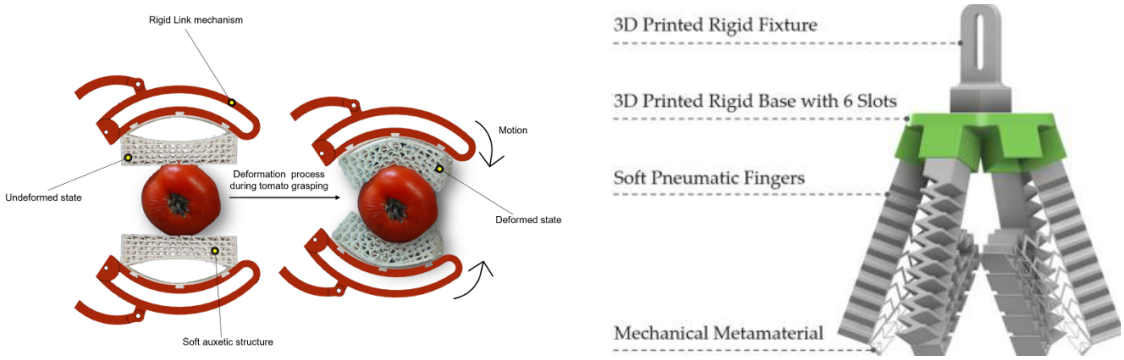

(a) Auxetic metamaterial-based soft gripper for tomato harvesting [24].

(b) Soft pneumatic gripper with integrated mechanical metamaterial [6].

Figure 5: Examples of soft grippers integrating mechanical metamaterials to enhance compliance and shape adaptation.

These examples demonstrate that mechanical metamaterials are a promising approach for enhancing compliance and shape adaptation in soft grippers for agricultural harvesting. However, existing designs are primarily limited to deformation-based mechanisms and do not enable controlled rotational motion of the gripper or the grasped object. Exploring the use of chiral mechanical metamaterials to generate rotational motion while maintaining controlled contact with the object motivates the work presented in this thesis.

3 Methods

3.1 Chiral Unit Cell Geometry and Column

3.1.1 Chiral Unit Cell Design

The chiral metamaterial investigated in this work is based on the design of Frenzel et al. [22]. During the development of the chiral unit cell, two unit cells with different geometric scaling were created and evaluated, as shown in Figure 6. While both configurations used the same chiral topology, they differed in the reference length used to define and scale the geometric parameters. Figure 6a shows the unit cell for which the parameters were scaled relative to a_z, representing the physical size of the unit cell as illustrated in Figure 4b. This produced a thinner structure with an arm angle δ of 22°. Figure 6b shows another unit cell, with parameters scaled relative to a, representing the lattice constant as illustrated in Figure 4b. This unit cell had a thicker structure and an arm angle δ of 34.8°. According to the results of the Bachelor's Integration Project by Alfonso [20], the arm thickness was the parameter that affected the twist response of the unit cell the most. Therefore, a unit cell with a thinner structure was evaluated. To adjust the geometric parameters while keeping the outer dimensions fixed, the parameters were defined relative to a_z instead of a. This ensured that both unit cells could be compared under identical external dimensions while varying the internal geometry.

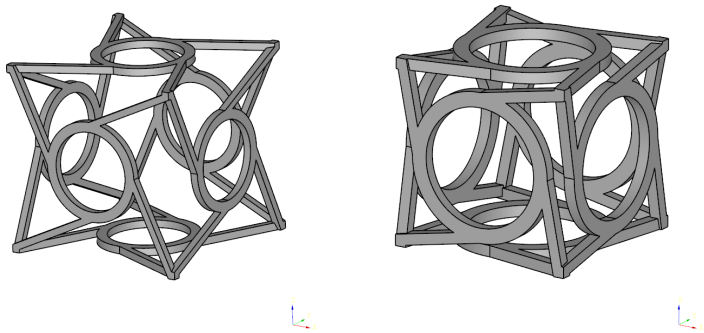

(a) Unit cell scaled by a_z. (b) Unit cell scaled by a.

Figure 6: Chiral unit cell geometries used in this thesis.

3.1.2 Chiral Column Design

The number of unit cells in the chiral column was chosen based on the research of Frenzel et al. [21]. They demonstrated that the highest twist response occurred in samples with $N = 1$, corresponding to a configuration of two left-handed and two right-handed unit cells stacked on top of each other. They used a mirror configuration to cancel the global rotation of the chiral column to measure the local twist of the unit cell. However, in this thesis, the global rotation is necessary, as it needs to be transferred from the chiral column to the arms of the gripper. Therefore, two units of a single-handedness were used, which corresponds to half of the $N = 1$ configuration of Frenzel et al. Figure 7 shows the chiral columns, each consisting of two left-handed stacked unit cells. Both columns were integrated into the gripper to evaluate and compare their influence on the rotating performance of the gripper. For clarity throughout the remainder of this report, the thinner column is referred to as Column A and the thicker column as Column B, as shown in Figures 7a and 7b, respectively.

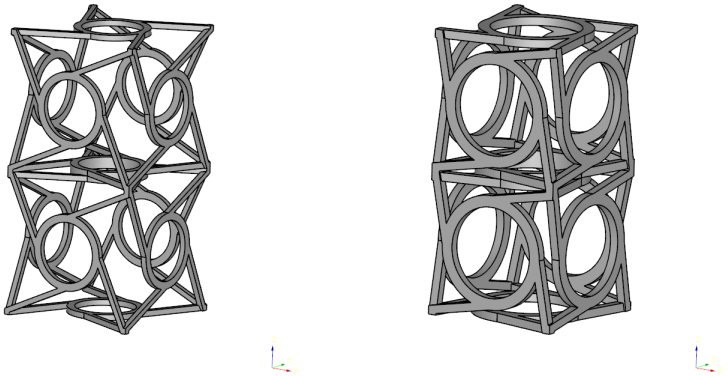

(a) Column A. (b) Column B.

Figure 7: Chiral columns used in this thesis.

3.2 Gripper Frame Geometry and Chiral Column Integration

3.2.1 Gripper Frame Geometry

The geometry of the gripper frame was designed based on the dimensions of a tomato, as shown in Figure 8. Since the average size of harvested tomatoes is approximately 55 mm, the U-shaped opening was designed to provide enough clearance for the tomato while allowing the arms to rotate inward during grasping. Therefore, the spacing between the arms was set to 70 mm to ensure that tomatoes with larger diameters could still be grasped and twisted. The height of the U-shaped opening was also set to 70 mm to ensure the tomato could be placed centrally without touching the gripper. The thickness of the gripper frame was set to 4 mm, and the width to 10 mm, to ensure a consistent stiffness throughout the frame. For the design of the gripper frame, a configuration of four fingers was chosen to obtain a fully symmetrical design. This configuration helped to maintain uniform contact around the tomato and limited its tendency to move out of the gripper during grasping. During actuation of the gripper, the lower legs served as a fixed support, and the upper arms rotated inward toward the center. This rotation was driven by the twist generated by the chiral column.

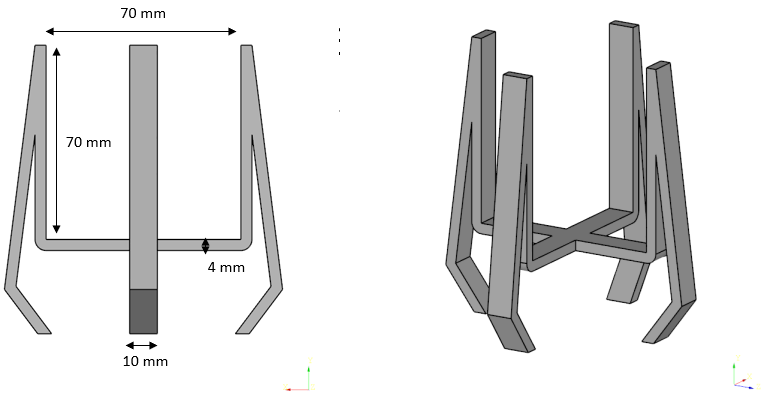

Figure 8: 2D and 3D view of the gripper frame.

3.2.2 Chiral Column Integration into the Gripper

During the development of the gripper, different placement strategies for the chiral column were explored in order to evaluate which configuration would result in the largest rotation of the gripper. The initial design was based on a small single chiral column positioned at the center of the gripper, with its upper surface fixed to the arms of the gripper, as shown in Figure 9a. Another configuration was explored by positioning four small chiral columns halfway or at the end of the arms, as shown in Figures 9b and 9c. In addition to varying the placement, several geometric modifications to the chiral column were explored. The cubic size of the chiral unit cell was increased to improve the connection between the column and the gripper arms. Another variation was created by rotating the column by 45° to align the corners of the column with the gripper arms. Furthermore, a trapezoidal column was explored, where the upper unit cell had different top and bottom surface dimensions. These variations, shown in Figure 10, were explored to study how geometric changes can affect the twist transmission from the column to the gripper.

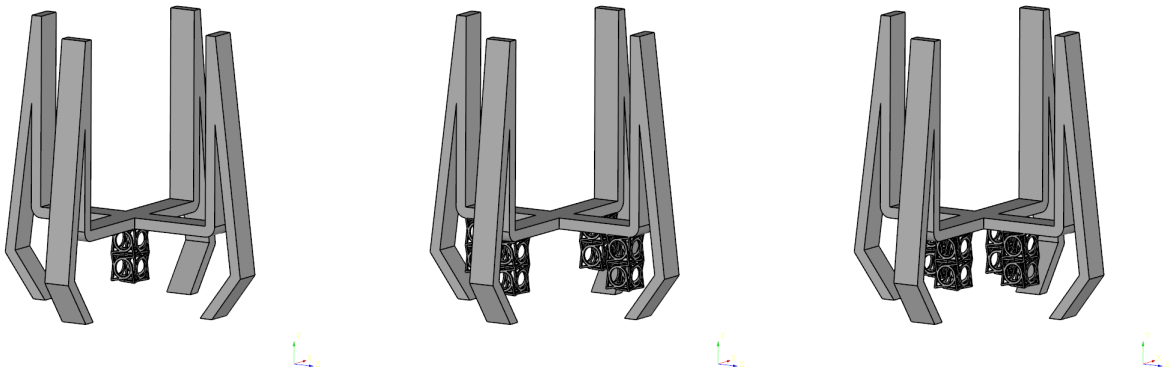

(a) Single central column. (b) Four columns at arm ends. (c) Mid-arm columns placement.

Figure 9: Placement strategies of a two-unit-cell 10x10x10 mm chiral column.

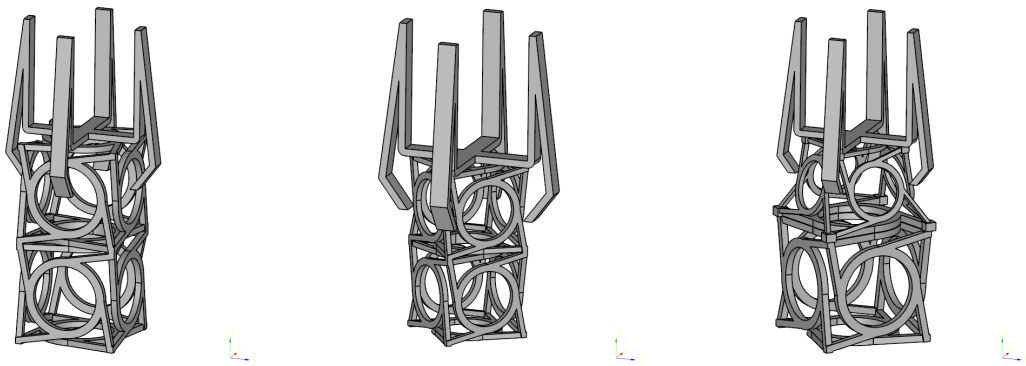

(a) 65×65x65 mm column. (b) Column rotated by 45°. (c) Trapezoidal column.

Figure 10: Geometric variations of the chiral column.

3.3 Software Tools

To perform finite element simulations on different gripper designs, the frame of the gripper and the column of the chiral unit cell were first modeled in Cadquery as separate files. By importing the chiral column file into the gripper frame file, the geometry and size of the chiral unit cell could be easily adjusted and integrated into the gripper. To perform simulations on the gripper designs, a STEP file was exported and then imported into Abaqus. For the models, a right-handed Cartesian coordinate system was used, and the geometry dimensions were defined in millimeters. The test object, a sphere representing a tomato, was created in Abaqus, as its geometry was simple enough to define within this software. Both models were then meshed, assigned material properties, and the contact interactions and boundary conditions were defined for the simulations. The data on the achieved rotation of both the gripper and the test object were exported from Abaqus, processed in Excel, and then imported into MATLAB to generate clear visualizations. The contact area and mean contact pressure between the gripper and the test object were visualized using a Python script. The CadQuery, MATLAB, and Python scripts used in this thesis are provided in Appendices A, B, and C, respectively.

3.4 Material Models

The gripper was assigned the Flexible 80A material in Abaqus, a hyperelastic elastomer often used in SLA 3D printing. To model Flexible 80A, the mass density was set to 1.18×10^{-9} tonne/mm^3. The material was defined as hyperelastic using a Mooney-Rivlin strain-energy potential. This model is widely utilized for elastomers and effectively captures the nonlinear behavior of rubber-like materials. Test data, as shown in Figure 11, was imported into Abaqus to show the hyperelastic response of Flexible 80A. The data consisted of uniaxial stress–strain measurements obtained from tensile experiments on Flexible 80A samples [25]. The hyperelastic material was assigned a Poisson's ratio of 0.13 to define the volumetric response. Abaqus then calculated the Mooney–Rivlin coefficients from the provided data to get an accurate representation of Flexible 80A's nonlinear behavior.

Initially, the test object was designed as a rigid sphere representing a tomato. The object was assigned a steel material and defined as a rigid body to ensure it remained non-deformable. This allowed for a focus on the rotation and contact conditions with the gripper without considering the object deformation. The test object was given a mass density of 7.85×10^{-9} tonne/mm^3, a Young's modulus of 2.1×10^5 MPa, and a Poisson's ratio of 0.3, corresponding to typical properties of steel.

To determine the rotation transferred to a deformable object, the rigid test object was replaced by a deformable sphere. A reduced Young's modulus of $E = 10$ MPa was selected to represent a soft, deformable object such as a tomato, while maintaining numerical stability in the simulations. The other material properties and modeling parameters were kept identical to the rigid case.

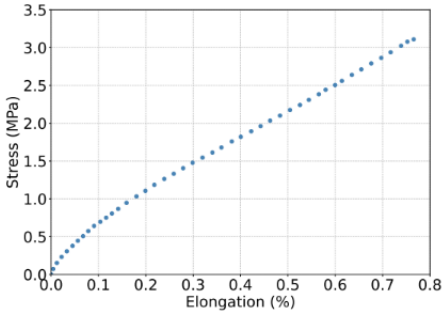

Figure 11: Data from tensile test of Flexible 80A samples [25].

3.5 Meshing Strategy

The quality of the mesh plays a crucial role in the accuracy and reliability of simulation results. A mesh that is too coarse can lead to inaccurate results, while an overly fine mesh significantly increases computational cost. When modeling hyperelastic materials, it is recommended to use hybrid elements [25]. Therefore, C3D10H elements have been used for the mesh of the gripper, which are 10-node quadratic tetrahedral hybrid elements especially designed for materials that experience large deformations. For the initial simulations involving only the gripper, a uniform global seed size of 4.4 mm was applied, providing sufficient accuracy while keeping computational cost manageable.

According to Spanos et al. [25], the gripper and object should ideally have a 4:1 ratio between the gripper's contact mesh size and the object's contact mesh size. This ratio provides a good balance between the reliability of the results and the computational costs of the simulations. However, for the initial simulations with the rigid object and the gripper, applying such a fine mesh to the entire sphere resulted in very long computation times. Since many simulations had to be performed to determine the placement of the object relative to the gripper, using this ratio would have been impractical. Therefore, a coarser ratio of 2:1 was used, resulting in a global seed size of 2.2 mm for the mesh of the object. It was meshed using C3D10 elements, which are 10-node tetrahedral elements that accurately represent the shape of the rigid object. Another measure taken to reduce computation time was making the object hollow, which helped decrease the number of mesh elements. The coarser ratio and hollow object significantly reduced computational cost. This setup still produced accurate results for the initial simulations, which primarily focused on the rotation of the object. In the later simulations, a finer mesh matching the 4:1 ratio proposed by Spanos et al. was used to improve the accuracy of the contact evaluation between the gripper and the object.

3.6 Contact Definition

The contact between the gripper and the object was defined using surface-to-surface contact with finite sliding, as it is more accurate than node-to-surface contact. The main surface was assigned to the test object, and the secondary surface to the inside of the gripper, which will be in contact with the object. For the normal behavior, hard contact and linear contact stiffness were applied. These properties prevent penetration between the surfaces and allow them to separate when no compressive normal force is acting between them. For the tangential behavior, two different friction conditions were examined in the simulations, depending on the objective. A friction coefficient of 0.4 was used to evaluate the rotation transfer and contact under realistic conditions. This value was selected to represent moderate dry friction, providing sufficient tangential resistance for rotation transfer without causing excessive sticking. In addition, frictionless contact was used to evaluate and compare the contact area and mean contact pressure, allowing the gripper fingers to freely slide along the surface of the object and adapt to its geometry. This configuration served as a reference for comparison with the frictional case, allowing the effect of tangential friction on the contact behavior to be evaluated.

3.7 Boundary Conditions and Loading

3.7.1 Boundary conditions and Actuation of the Gripper

Boundary conditions can significantly influence simulation results, as they determine how a model is constrained and how external loads are transferred through a structure. Therefore, two different setups for the boundary conditions were examined in the simulations involving only the gripper. These setups were used to study how the constraints affected the deformation of the chiral column and the rotation

transferred to the gripper. In both setups, the lower parts of the gripper legs were modeled as encastre supports, as shown in Figure 12a, meaning that they were fully fixed and unable to translate or rotate during the simulations. On the chiral column, the two setups differed in their constraints and loading application.

In the first boundary condition setup, shown in Figure 12b, the bottom face of the chiral column was fixed in translation in the x-,y-, and z- directions, and in rotation about the x- and z- axes. At the bottom face, a vertical displacement was applied downwards to observe how the applied loading affects the rotation transferred from the chiral column to the gripper. This setup was chosen for evaluation, as it allowed the base of the chiral column to rotate freely about the y-axis, while restricting all other degrees of freedom. Therefore, it was expected that the deformation of the chiral column would be transferred mostly to the gripper in the form of rotational motion.

In the second boundary condition setup, shown in Figure 12c, the bottom surface was pinned, meaning that the translations in the x,y, and z directions were fixed. Unlike the first setup, where the displacement was applied at the bottom surface, the displacement was applied at the top surface of the chiral column. Since the column's base was unable to move, the deformation of the column caused by the loading was expected to be fully transferred to the gripper. This setup was used to examine how applying the load at the top surface affected the rotation transferred from the chiral column to the gripper. In practice, this boundary condition setup is comparable to the actuation setup presented by Eusterbrock [26]. In that design, the soft gripper is mounted on a rigid frame and actuated by a stepper motor that applies a vertical displacement via a cable-driven mechanism while the base remains fixed. Similarly, in the design presented in this research, the base of the chiral column would be fixed and actuated from the top in a manner comparable to that described by Eusterbrock.

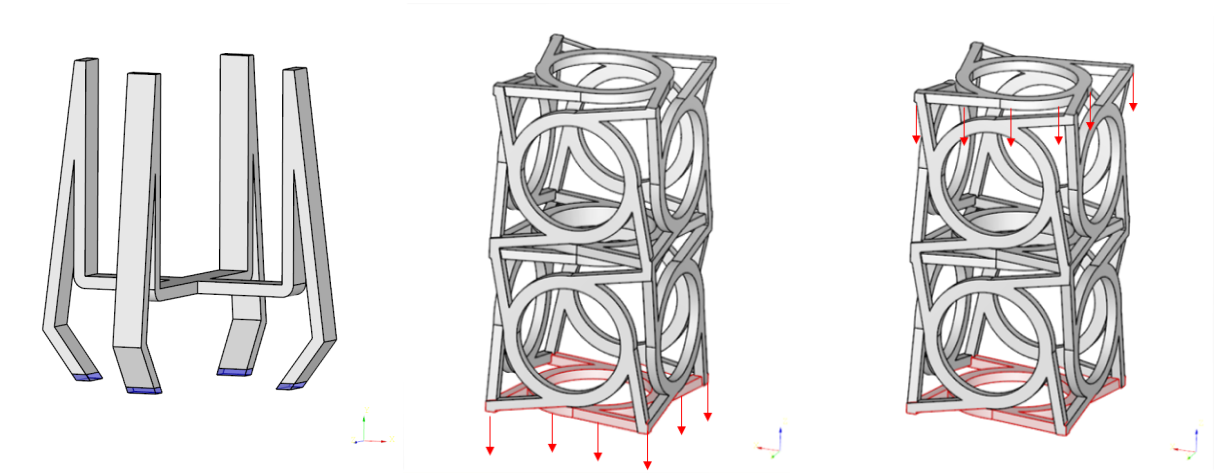

(a) Encastre supports on gripper. (b) Boundary conditions setup 1. (c) Boundary conditions setup 2.

Figure 12: Boundary condition configurations used in the simulations.

3.7.2 Boundary conditions on the Sphere

To constrain the spherical test object, two different boundary condition approaches were used, depending on the objective of the simulation. For the simulations evaluating rotational motion transfer and contact under frictional contact conditions, a reference point was defined at the middle of the sphere and coupled kinematically to the inner surface of the sphere. The reference point was constrained by fixing all translational degrees of freedom and restricting rotation about the x and z-axes.

This approach ensured that the sphere remained positionally fixed while allowing rotation about the y-axis resulting from contact with the gripper. For the reference simulations using frictionless contact, the inner surface of the sphere was pinned to constrain all translational degrees of freedom of the test object. This approach prevented rotational motion of the sphere, allowing the contact area and mean contact pressure to be evaluated without the influence of rotational effects.

3.8 Computation of Rotation Angles

3.8.1 Gripper Rotation

To compare the performance of the gripper designs, the rotation angle of each gripper was computed from the simulation results. The rotation angle was used as a quantitative metric to evaluate how effectively the deformation of the chiral column was converted into rotational motion of the gripper. Based on this comparison, the design that achieved the largest rotation was selected.

The rotation of the gripper was quantified by tracking the displacement of a reference node located at the end of one gripper arm, as shown in Figure 13a. This location for the node was chosen as it lies at a fixed radial distance from the vertical rotation axis of the gripper. This allowed the rotational motion of the gripper to be evaluated consistently across different simulations. The reference node was initially positioned at $x = 0$ mm and $z = -35$ mm, placing it on a circular path around the gripper's vertical rotation axis at a radius of $r = 35$ mm. During deformation, this radius was assumed to remain constant as the displacement in the z-direction was negligible. Because the node was positioned on the negative z-axis, rotation about the vertical axis was fully described by its displacement in the x-direction. The z-coordinate remained approximately constant at the rotation radius and therefore did not need to be included in the angle calculation. The rotation angle about the y-axis was computed using Eq. (1), and a schematic of the calculation method is shown in Figure 13b.

$$\theta = \arctan\left(\frac{\Delta x}{r}\right), \tag{1}$$

where Δx is the displacement of the reference node in the x-direction and r is the radial distance from the vertical rotation axis. Since Abaqus reports angular quantities in radians, the computed rotation angles were converted to degrees using a factor of $\frac{180}{\pi}$.

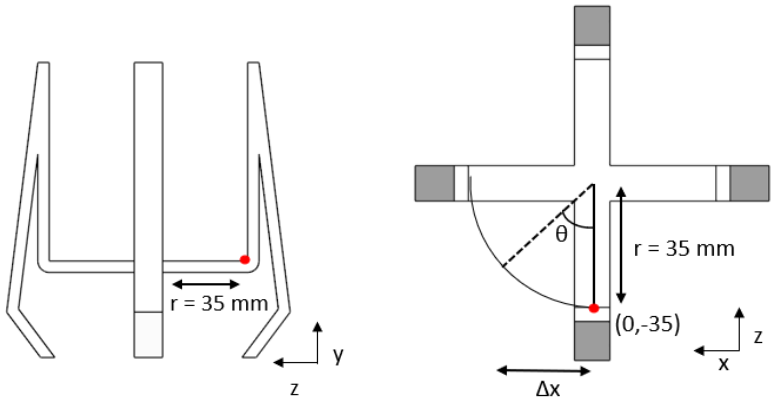

(a) Reference node position. (b) Rotation angle calculation.

Figure 13: Visualization of the reference node position and the method used to compute the gripper rotation angle.

3.8.2 Test Object Rotation

After the best performing gripper design was selected, the effect of object placement on the transferred rotation was evaluated. This analysis was performed using a rigid test object. Based on the optimal placement of the object, the rotation of a deformable test object was examined.

For the computation of the rotation angle of the rigid test object, the same approach was used as for the gripper. The rotation angle was calculated from a reference point located at a fixed radial distance from the rotation axis. In this case, the radial distance r was equal to the radius of the test object, as the rigid object does not deform. The reference node was positioned at half the height of the spherical test object, at $x = 0$ mm and $z = -r$ mm. The rotation angle was computed from the horizontal displacement of this reference node.

The same calculation method was used for the deformable test object. As the deformation of the object was sufficiently small within the applied displacement range, the distance between the reference node and the y-axis was assumed to remain fixed. Therefore, the displacement of the reference node was used to calculate the rotation of the deformable object.

3.9 Contact Area and Mean Contact Pressure

Beyond the rotation angle achieved by the gripper and the object, it was important to assess whether continuous contact was maintained between the gripper and the object during grasping and twisting. This assessment was necessary, as the effective transfer of rotation relies on sufficient and continuous contact between the gripper and the test object. To evaluate the quality of the contact interaction, the contact area and mean contact pressure were analyzed.

The contact area represents the amount of physical contact between the gripper fingers and the object in mm^2. It was computed by summing the contact area contributions of all nodes in contact at the interface for each increment. The mean contact pressure denotes the average normal pressure over the active contact area between the gripper fingers and the test object. It was computed by averaging the contact pressure values of all nodes that were active at the contact interface at each increment. The contact area and mean contact pressure were evaluated for both rigid and deformable test objects, and for both frictional and frictionless contact conditions. The behavior of the contact area and mean contact pressure over the applied displacement range provided insights into how the contact developed during grasping and twisting.

4 Results

In the previous chapter, the methods required to model the gripper designs and to perform the simulations were discussed. This section presents the results obtained from these simulations and a quantitative comparison of the different gripper designs. First, the appropriate boundary conditions are identified and selected to ensure a consistent simulation setup across all analyses. Thereafter, different gripper designs are evaluated by varying the geometry of the chiral column while keeping the gripper frame identical for all simulations. The influence of the position, size, and orientation on the rotational response of the gripper is analyzed. Based on this analysis, the design that achieved the largest rotational response is selected for further analysis. The selected gripper is then used to investigate whether the rotational motion of the gripper can be transferred to a rigid test object. This is examined for a rigid object at different positions. The most effective configuration is used to further analyze the rotational response and contact behavior of a deformable test object. For both the rigid and the deformable test object, the contact behavior is assessed by evaluating the contact area and mean contact pressure.

4.1 Factors Influencing Gripper Rotation

4.1.1 Boundary Conditions

The first important step in the simulations was to determine the appropriate boundary conditions for the gripper. Therefore, two boundary conditions were considered to evaluate their influence on the rotational response. Figure 14 shows the achieved rotation angle as a function of the applied displacement of 5 mm for both boundary conditions. The results correspond to a gripper with Column A, shown in Figure 7a, with unit cell dimensions of $10 \times 10 \times 10$ mm. For both boundary conditions, the rotation angle increased as the applied displacement increased. This shows that for both cases, the deformation of the chiral column was transferred into a rotational motion of the gripper. However, a clear distinction between the two boundary conditions was observed. The rotation angle of the gripper for Boundary Condition 2 was significantly larger than for Boundary Condition 1 over the entire displacement range. At the maximum applied displacement, the gripper reached a rotation angle of approximately 0.29° for Boundary Condition 2 and a rotation angle of approximately 0.047° for Boundary Condition 1. This difference was caused by the constraints of the boundary conditions. In Boundary Condition 2, most of the applied displacement was converted into deformation of the chiral column, while in Boundary Condition 1, part of the displacement was absorbed through downward motion of the gripper base, leading to a smaller rotational response. A similar trend was observed for larger chiral column sizes, where Boundary Condition 2 consistently resulted in higher rotation angles than Boundary Condition 1, as shown in Table 2. Based on these results, Boundary Condition 2 was used for all subsequent simulations.

Table 2: Rotation angle for different unit cell sizes under both boundary conditions at an applied displacement of 5 mm.

Chiral column unit cell size [mm]	Boundary Condition 1 [°]	Boundary Condition 2 [°]
10	0.047	0.29
20	0.14	0.36
65	1.14	1.83

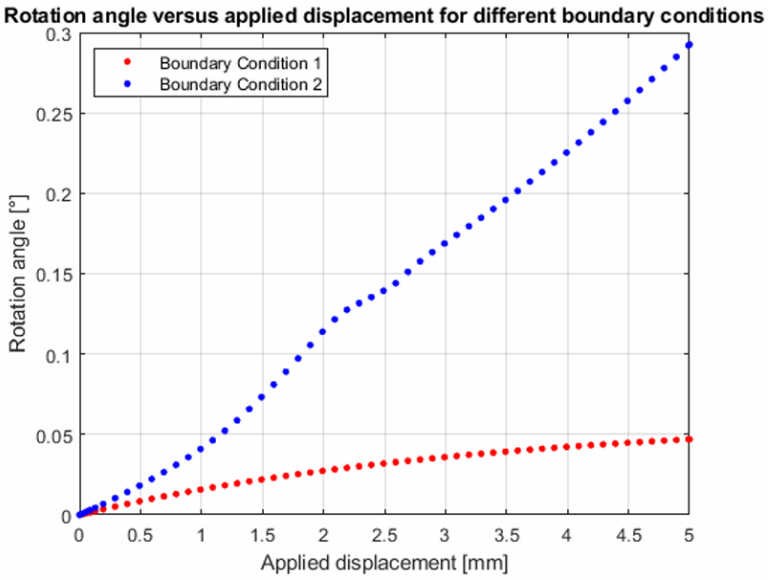

Figure 14: Rotation angle as a function of the applied displacement for a gripper using Column A ($10 \times 10 \times 10$ mm) under two different boundary conditions.

4.1.2 Chiral Column Placement

The influence of the placement of the chiral column on the rotational response of the gripper was evaluated using Column A, with unit cell dimensions of $10 \times 10 \times 10$ mm. Using the same chiral column for the different placement designs allowed for a consistent evaluation of the effect of column placement on gripper rotation. Three placement configurations were evaluated, as previously shown in Figure 9: a single column positioned at the center of the gripper, four columns positioned in the middle of the gripper arms, and four columns positioned at the end of the gripper arms.

The rotation angles versus the applied displacement for the three placement configurations are shown in Figure 15. The rotation angles of the three configurations were compared up to an applied displacement of 2 mm. This displacement was chosen for comparison as the configurations with four columns did not converge when larger displacements were applied. In particular, the configuration with the columns positioned at the end of the arms did not converge beyond an applied displacement of 2 mm. The configuration with four columns positioned at the midpoints of the gripper did not converge beyond an applied displacement of approximately 1.65 mm. Due to these convergence limitations, the comparison was restricted to the displacement range for which simulation results were available.

Figure 15 shows that for small applied displacements, the configurations with four columns achieved a larger rotation angle compared to the single-column configuration. Furthermore, these configurations exhibited a steeper initial increase in rotation. However, for the four-column configurations, the rotation angle begins to level off beyond a certain displacement, whereas the single-column configuration continues to exhibit an increasing rotation angle. Within the converged displacement range, the configurations with four columns achieved rotation angles of approximately 0.17° and 0.12°, while the single-column configuration achieved a rotation angle of approximately 0.11°. Due to the limited convergence of the four-column configurations at larger applied displacements, their maximum achievable rotation could not be evaluated. In contrast, the single-column configuration could be evaluated for larger applied displacements and exhibited stable convergence as previously shown in Figure 14. Therefore, the single-column configuration was selected for further analyses.

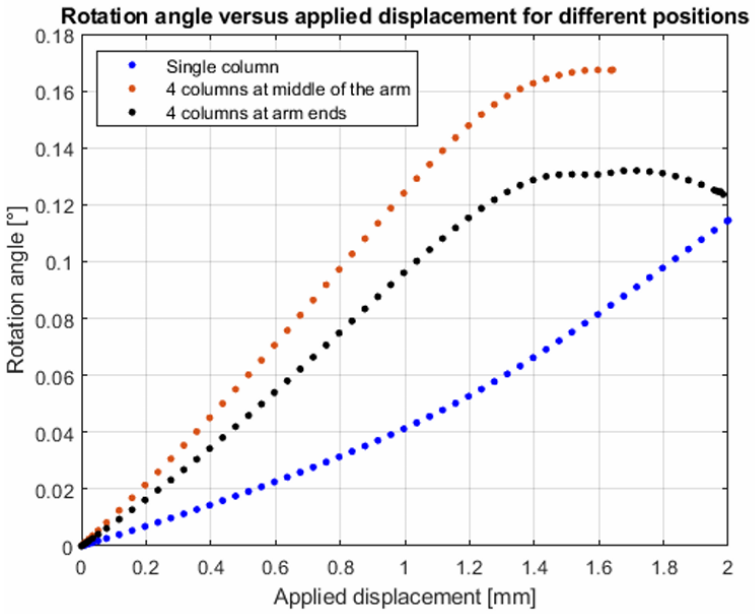

Figure 15: Rotation angle versus applied displacement for a gripper using Column A ($10 \times 10 \times 10$ mm) for different placement strategies.

4.1.3 Unit Cell Size and Thickness

After the single-column configuration was selected as the most suitable placement, the influence of the size and thickness of the unit cell on the rotational response of the gripper was evaluated. Simulations were performed on gripper designs with different unit cell sizes for Columns A and B, as previously shown in Figure 7, where the corresponding chiral column geometries are illustrated. Figures 16 and 17 show the rotation angles as a function of the applied displacement for three different unit cell sizes for Columns A and B, respectively.

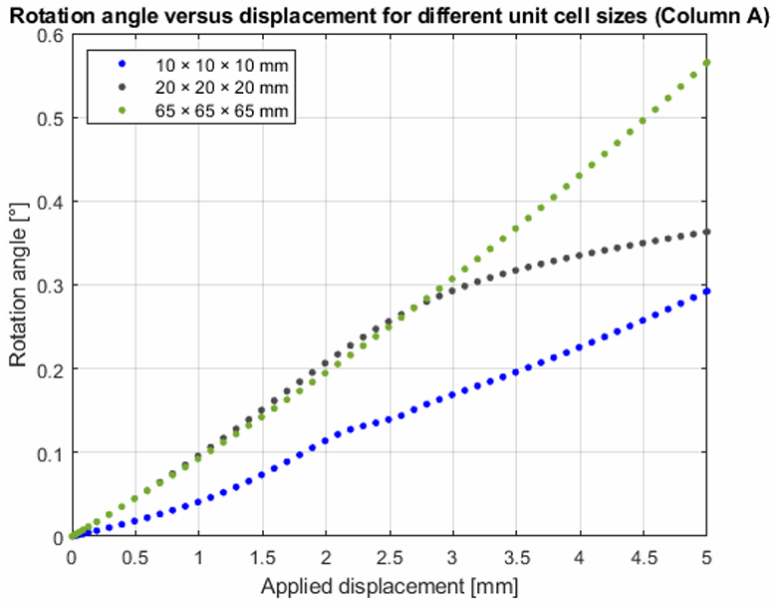

Figure 16: Rotation angle versus applied displacement for different unit cell sizes (Column A).

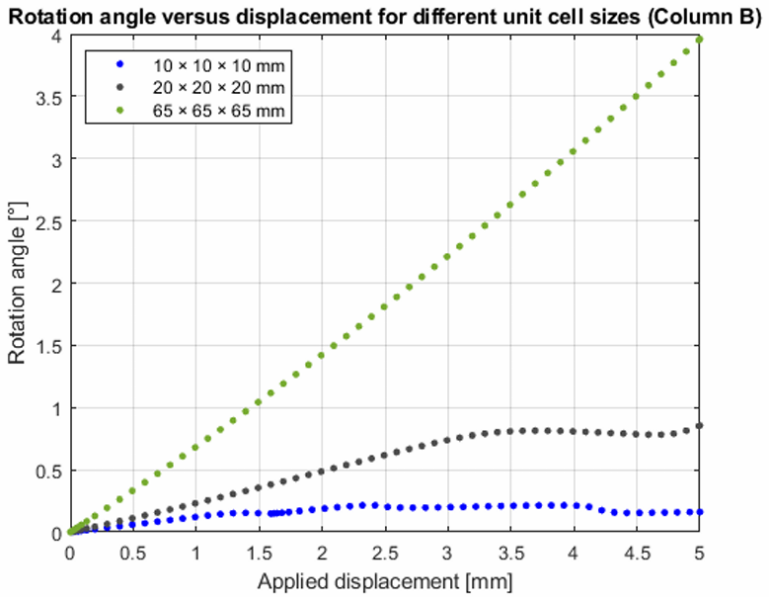

Figure 17: Rotation angle versus applied displacement for different unit-cell sizes (Column B).

For Column A, the rotational response of the gripper for the three unit cell sizes is shown in Figure 16. The smallest unit cell size ($10 \times 10 \times 10$ mm) demonstrated the lowest rotational response and achieved a rotation angle of approximately 0.29° after an applied displacement of 5 mm. The intermediate unit cell size ($20 \times 20 \times 20$ mm) demonstrated a higher rotational response, reaching a rotation angle of approximately 0.36° at the same applied displacement. The largest unit cell size ($65 \times 65 \times 65$ mm) achieved the highest rotation angle of approximately 0.57°. These results indicate that increasing the unit cell size leads to an increased rotational response for Column A. For Column B, the rotational response of the gripper for the three unit cell sizes is shown in Figure 17. A similar trend to that observed for Column A is present, with an increased unit cell size leading to higher rotation angles. At an applied displacement of 5 mm, the smallest unit cell achieved a rotation angle of approximately 0.16°, and the intermediate unit cell size reached approximately 0.85°. The largest unit cell achieved the highest rotational angle of approximately 3.96°.

For Columns A and B, the largest unit cell achieved the highest rotation angle of the gripper. The size of this largest unit cell ($65 \times 65 \times 65$ mm) represents the maximum size that could be fitted within the dimensions of the gripper frame. When comparing both configurations at identical unit cell sizes, grippers with Column B consistently achieved larger rotation angles than those with Column A. This difference increased for larger unit cell sizes and was greatest for the largest configuration. Based on these results, Column B was selected for subsequent analyses, with a focus on larger unit cell sizes, and was therefore adopted in the following sections.

4.1.4 Column Orientation

After Column B and large unit cell sizes were identified as the most suitable configuration, the influence of the orientation of the chiral column on the rotational response of the gripper was investigated. In comparison to the original orientation, the chiral column was rotated 45 degrees such that the corners of the top face of the column were aligned with the gripper arms, as shown in Figure 10b. This orientation was considered because the corners of the chiral column experience large displacements during deformation. By aligning these corners with the gripper arms, the deformation was expected

to be more effectively converted into the rotational motion of the gripper. Due to this rotated configuration, a unit cell size of $48 \times 48 \times 48$ mm was selected as it was the largest size that fitted within the dimensions of the gripper frame when rotated 45°.

Figure 18 shows the rotation angle as a function of the applied displacement for both orientations. The rotation angle of the gripper increased for both with increasing applied displacement. However, the rotated configuration experienced a steeper increase in rotation angle over the entire displacement range. At an applied displacement of 5 mm, the original orientation achieved a rotation angle of approximately 3.96°, while the rotated orientation achieved an angle of approximately 4.96°. These results indicate that, despite the reduced unit cell size, rotating the chiral column by 45° significantly enhanced the rotational response of the gripper.

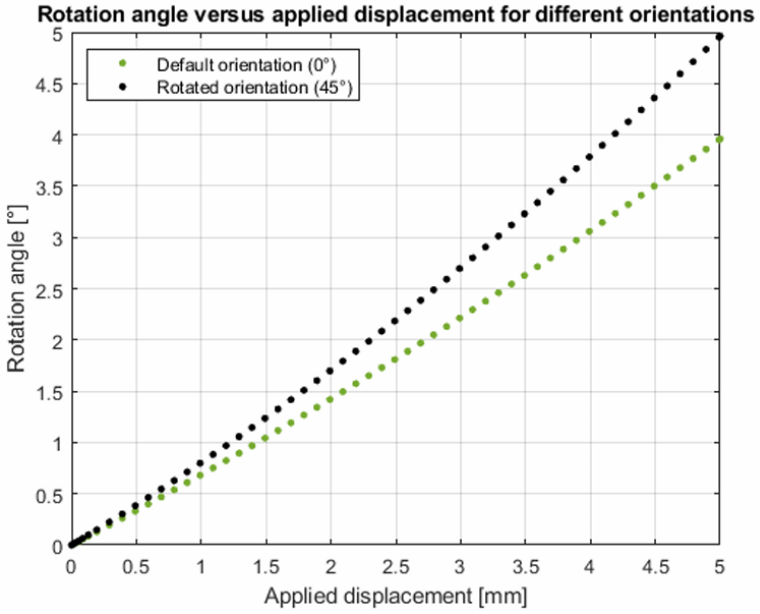

Figure 18: Rotation angle versus the applied displacement for different column orientations.

4.1.5 Trapezoidal Column

To combine the influence of a large unit cell size and column orientation, a trapezoidal column geometry was introduced, as shown in Figure 10c. In Section 4.1.3, it was concluded that larger unit cell sizes resulted in higher rotation angles of the gripper. Due to the rotated orientation, the maximum feasible unit cell size was reduced. To address this limitation, a trapezoidal chiral column was investigated. In this design, a large unit cell of size $72 \times 72 \times 72$ mm was placed at the base of the column. On top of this base unit cell, a trapezoidal unit cell was placed with a height of 48 mm, a base cross-section of 72×72 mm, and a top cross-section of 48×48 mm.

Figure 19 shows, for both the rectangular chiral column and the trapezoidal chiral column at a 45° orientation, the rotational angle as a function of the applied displacement. As the applied displacement increased, the difference in rotation angle between the two configurations increased, in favor of the rectangular chiral column. At an applied displacement of 5 mm, the rectangular chiral column achieved a rotation angle of approximately 4.96°, while the trapezoidal chiral column reached a rotation angle of approximately 3.84°. A possible explanation for this result is that the larger unit cell increased the stiffness of the lower part of the column, which limited the overall deformation of the column. Therefore, the trapezoidal configuration was not used in subsequent analyses.

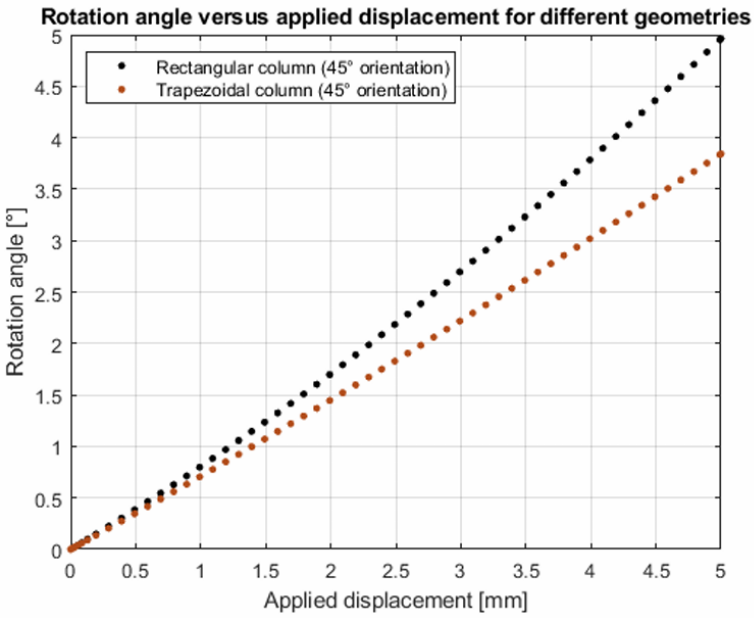

Figure 19: Rotation angle versus applied displacement for a rectangular and a trapezoidal column.

4.1.6 Number of Stacked Unit Cells and Applied Displacement

Based on the results of the previous sections, the selected gripper configuration with two stacked unit cells of $48 \times 48 \times 48$ mm achieved the highest rotational response of the gripper. In Section 3.1.2, it was assumed that, based on the paper by Frenzel et al. [21], two stacked unit cells would achieve the highest rotational response. To verify this assumption, the same configuration was evaluated using four stacked unit cells. Figure 21 confirmed this assumption, as the configuration with two stacked unit cells achieved a higher rotational angle than the configuration with four stacked unit cells. At an applied displacement of 5 mm, the two-unit cell configuration reached a rotation angle that was nearly twice as large as the four-unit cell configuration.

The resulting final gripper design, therefore, consists of a single Column B oriented at 45°, with two stacked unit cells of $48 \times 48 \times 48$ mm, as shown in Figure 20, and was used in all subsequent simulations. First, its behavior under larger applied displacements was evaluated.

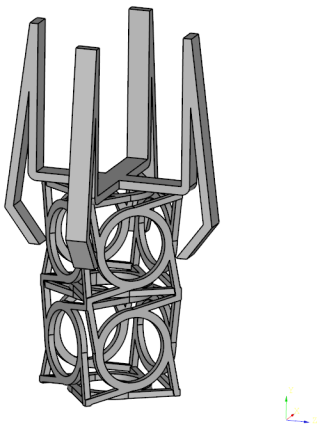

Figure 20: Final gripper design. Column B oriented at 45°, with two unit cells of $48 \times 48 \times 48$ mm.

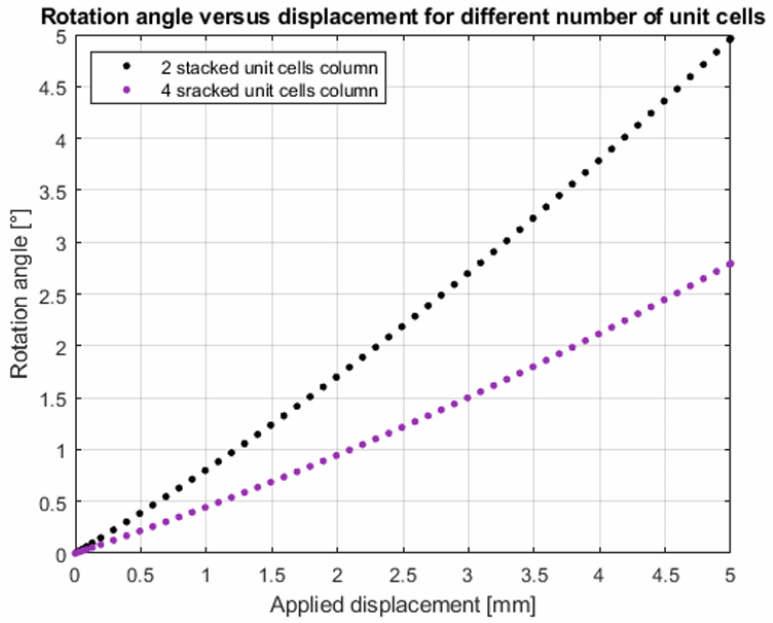

Figure 21: Rotation angle versus applied displacement for gripper configurations with two and four stacked unit cells.

A displacement of 20 mm was applied to show the rotational response of the final gripper design for larger displacements. Figure 22 shows that the rotation initially increased with the increasing applied displacement. At a displacement around 12.5 mm, the rotation angle reached a maximum, after which it remained approximately constant at a rotational angle of 12.68°. This indicated that further increasing the applied displacement did not result in additional deformation of the chiral column. Therefore, applying displacements greater than 12.5 mm did not lead to a higher rotation angle.

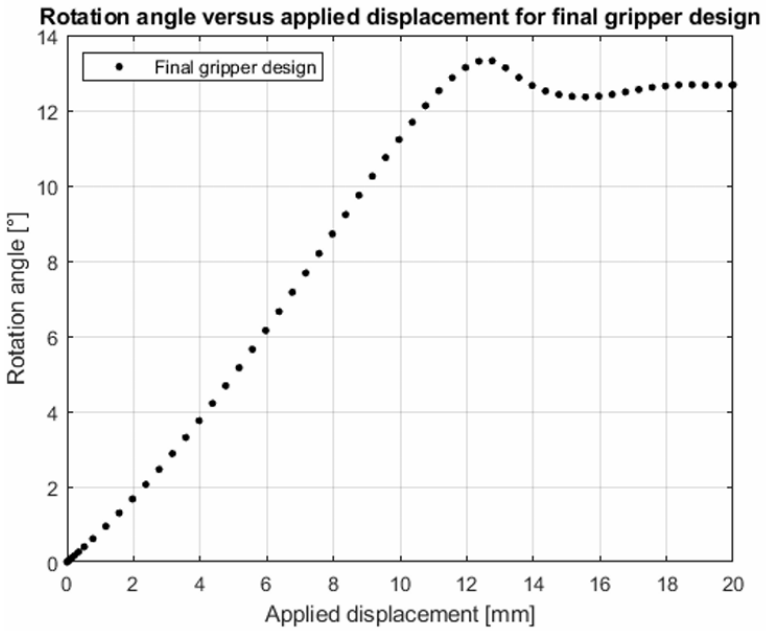

Figure 22: Rotation angle versus applied displacement for the final gripper design.

4.2 Rotation Transfer to the Test Object

4.2.1 Rigid Test Object

For the simulations, a rigid spherical test object with a diameter of 55 mm, corresponding to the average diameter of a tomato, was used. Several simulations were performed in which the test object was positioned at different heights relative to the gripper to determine the position that most effectively transferred the rotational motion from the gripper to the test object. Three vertical positions of the test object relative to the gripper were evaluated, namely at $y = 0$ mm, where the object was positioned very close to the gripper arms without initial contact, and at $y = 10$ mm and $y = 20$ mm above this position. For each position, a displacement of 5 mm and 10 mm was applied. The simulation setup is illustrated in Figure 23.

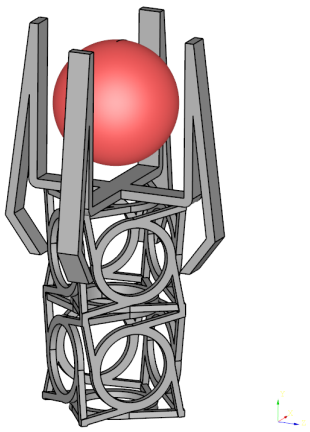

Figure 23: Simulation setup of the gripper and rigid spherical test object for the position $y = 10$ mm.

Most simulations did not converge over the full applied displacement range due to numerical instabilities related to the contact between the gripper and the rigid test object. Therefore, a comparison of the maximum achieved rotation could not be made for all configurations. To ensure a consistent comparison, the slope of the rotation-displacement curve was determined by fitting a linear trend through the data between the point at which the object began to rotate and the last converged increment. This slope was used to assess how effectively the rotational motion was transferred to the test object.

In all simulations, rotation of the rigid test object was achieved. The slope, representing the rate of change of the rotation angle of the object per mm of applied displacement, is summarized in Table 3. Only the results for an applied displacement of 10 mm are reported, as this case converged over a larger displacement range than the 5 mm simulations. The table shows that only small differences existed in the calculated slope between the three positions. Since there was no consistent trend observed, no single object position could be identified as most effective for transferring rotational motion.

Table 3: Slopes of the rotation–displacement curves for the rigid test object.

Object position y [mm]	Applied displacement [mm]	Slope [°/mm]
0	10	2.26
10	10	2.16
20	10	2.22

Figure 24, shows the rotational response of the rigid test object at the three vertical positions for an applied displacement of 10 mm. The x-axis starts at 2 mm, as no contact between the gripper and the object was made before this displacement. It can be observed that as the object was positioned vertically higher, it came into contact with the gripper at lower applied displacements, but also lost numerical convergence earlier. By comparing the displacement range over which rotation occurred, the configuration with the object positioned at $y = 10$ mm exhibited the longest convergence period. This configuration was therefore selected for the subsequent analysis.

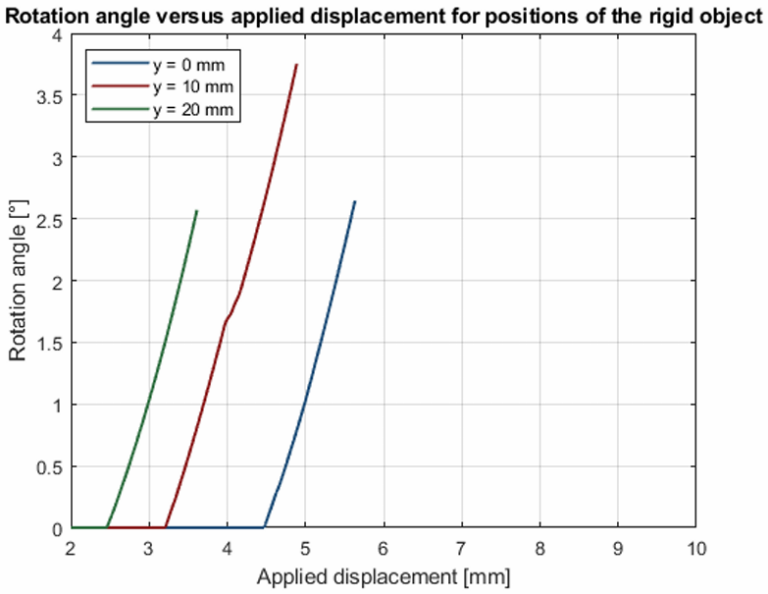

Figure 24: Rotation angle versus applied displacement for different positions of the rigid object.

4.2.2 Deformable Test Object

The previous section demonstrated that rotation could be transferred to a rigid test object. In this section, the same configuration is used, positioned at $y = 10$ mm, to evaluate whether rotation could also be transferred to a deformable test object. To improve numerical stability, a 10 mm displacement was applied in the simulation, which converged up to approximately 9 mm. This enabled the rotational response to be evaluated over a larger displacement range than for the rigid test object. Over the converged displacement range, the deformable object reached a rotation angle of approximately 31.32°, demonstrating effective transfer of rotational motion from the gripper. While Section 4.1 reports the rotation of the gripper arms, the rotation of the test object resulted from the tangential motion of the fingers at the contact interface, which experienced a larger effective rotation than the gripper arms.

Figure 25 shows the rotation angle of the deformable test object as a function of the applied displacement over a range from 3 to 10 mm, as no contact between the gripper and object occurred before an applied displacement of 3 mm. The rotational responses of the rigid and deformable test objects closely followed each other, indicating similar rotational behavior under comparable contact conditions. The simulation of the deformable object converged over a longer displacement range than the rigid object, which can be explained by the reduced stiffness of the deformable object, leading to smoother contact interactions. Beyond the convergence limit of the rigid test object, the deformable object continued to rotate, reaching larger rotation angles. To further investigate the interaction between the gripper and the test object, the following section examines the contact area and contact pressure under frictional and frictionless contact conditions.

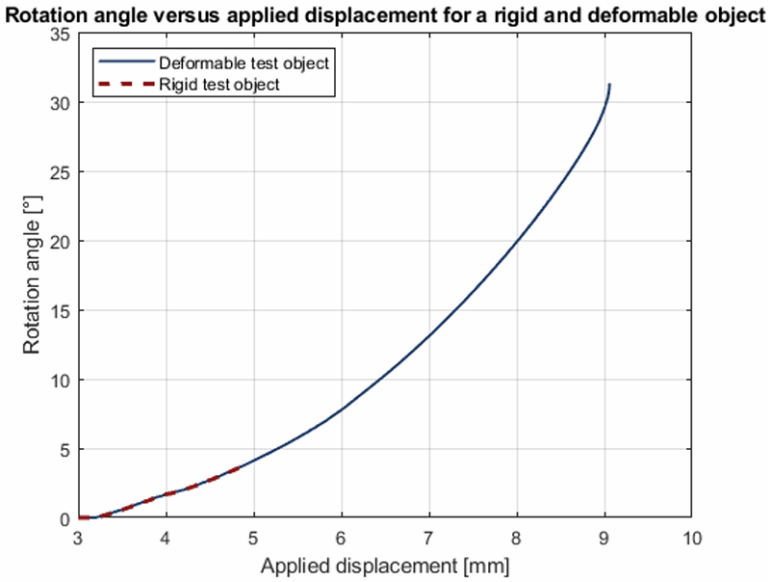

Figure 25: Rotation angle versus applied displacement for a rigid and deformable test object.

4.3 Contact Between Gripper and Test Object

The results in Section 4.2 demonstrated that rotational motion was successfully transferred from the gripper to both a rigid and a deformable object. This transfer occurred through frictional contact at the interface between the gripper fingers and the object. To assess the contact during the grasping and twisting of the object, the behavior of the contact area and the mean contact pressure are examined and compared in this section for both frictional and frictionless contact conditions.

4.3.1 Frictional Contact Conditions

In Section 4.2, a friction coefficient of $\mu = 0.4$ was applied between the gripper fingers and the test object to represent a realistic frictional interaction. In this subsection, the same friction coefficient is used to evaluate the resulting contact behavior by examining the contact area and the mean contact pressure during grasping and twisting.

Figure 26a shows the contact area as a function of the applied displacement. For both cases, the contact area experienced a rapid increase upon contact initiation, reaching a maximum shortly thereafter. After this peak, the contact area rapidly decreased and stabilized around 11.5 mm^2 for both cases. The simulation for the rigid object converged up to an applied displacement of approximately 4.5 mm. Within this interval, the contact area followed a behavior similar to that observed for the deformable object, with a few localized deviations from the overall behavior. Beyond this applied displacement, the contact area could only be evaluated for the deformable object, which remained approximately constant around 11.5 mm^2 for most of the remaining displacement range. A temporary increase in contact area was observed around an applied displacement of 6 mm, after which it returned to the stabilized value. Toward the end of the simulation, a small increase in contact area was observed, after which the results terminate at an applied displacement of approximately 9 mm.

Figure 26b shows the mean contact pressure as a function of the applied displacement. After contact initiation, the mean contact pressure increased for both the rigid and deformable objects. Within the displacement range over which the rigid-object simulation converged, both cases showed similar behavior, with only small local deviations for the rigid case. For the deformable object, the mean

contact pressure exhibited an overall increasing trend with local fluctuations. Toward the end of the simulation, the mean contact pressure decreased with small variations until convergence was lost.

Overall, the results show that contact was maintained throughout most of the simulations, with the contact area remaining approximately constant and the mean contact pressure increasing with the applied displacement. These observations indicate that the interaction between the gripper and the object remains continuous and develops gradually during most of the twisting.

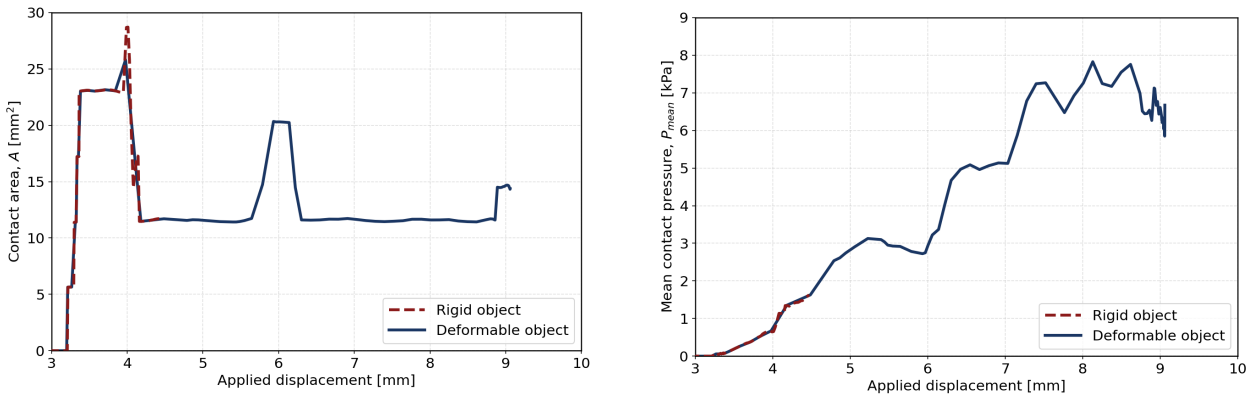

(a) (b)

Figure 26: Contact area and mean contact pressure versus applied displacement for a rigid and a deformable test object under frictional contact conditions with a friction coefficient of $\mu = 0.4$.

4.3.2 Frictionless Contact

The simulations with frictionless contact, in which rotation of the test object was not permitted, were used as a reference case to assess the influence of friction on the contact behavior. In these simulations, the tangential frictional forces were removed, allowing the gripper fingers to freely slide along the surface of the object and adapt to its geometry through normal contact interactions alone. The frictionless case, therefore, represents an idealized scenario in which the contact area and mean contact pressure were determined solely by the applied displacement and the resulting deformation of gripper fingers and the test object, without the influence of frictional effects.

Figure 27 shows the contact area and mean contact pressure as a function of the applied displacement for the rigid and deformable test objects under frictionless contact conditions. In the case of the contact area, both objects exhibited a steep increase after contact initiation, after which the contact area stabilized around 11.5 mm^2, with two local peaks occurring at higher displacements. Minor differences were observed, such as the timing of these local peaks, with the rigid object reaching these peaks slightly earlier than the deformable object. For both test objects, the mean contact pressure increased with applied displacement, with similar behavior observed in both cases. The rigid object, however, showed some fluctuations and peaks and valleys at earlier displacements with slightly different mean contact pressure values.

The contact behavior obtained under frictionless and frictional conditions was compared to assess the influence of tangential friction on the interaction between the gripper and the test object. The frictionless simulations fully converged for both the rigid and deformable test objects, due to the absence of tangential friction and the restriction of test object rotation. For the rigid test object, numerical convergence was achieved only over a limited displacement range. Therefore, the deformable test object is used for a comparison of frictional and frictionless contact behavior.

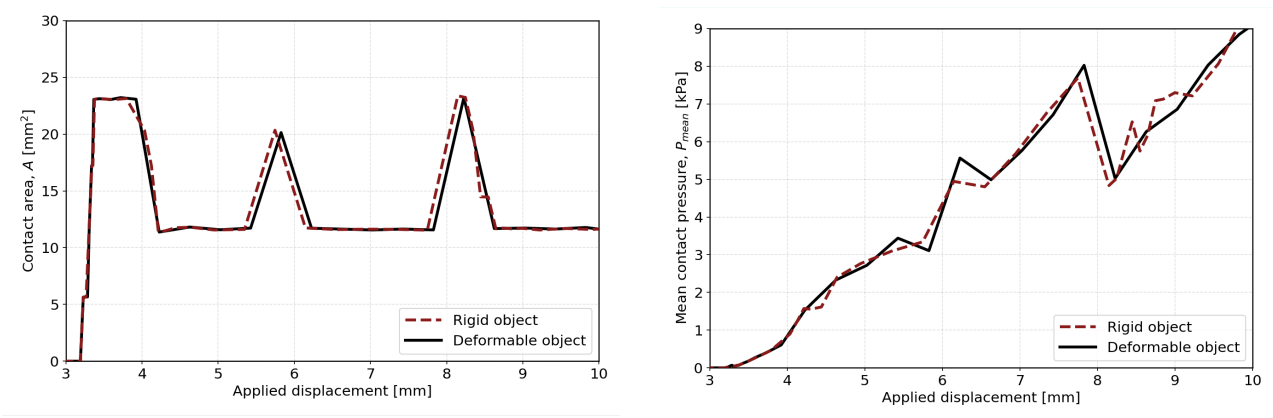

(a) (b)

Figure 27: Contact area and mean contact pressure versus applied displacement for a rigid and a deformable test object under frictionless contact.

Figure 28 shows the contact area and mean contact pressure as a function of the applied displacement for a deformable test object under frictional and frictionless contact conditions. Within the displacement range where both simulations converged, similar trends in contact area and mean contact pressure were observed for the frictional and frictionless cases. For both cases, the contact area increased rapidly after contact initiation to a similar value and subsequently stabilized around 11.5 mm^2, after which local peaks were observed. For the frictionless case, these local peaks occurred at slightly lower applied displacements than in the frictional case, indicating an earlier redistribution of contact. For the mean contact pressure, both the frictional and frictionless cases exhibited an increasing trend with applied displacement. In the frictionless case, local peaks and valleys occurred at slightly lower applied displacements and reached higher values, resulting in an overall higher curve compared to the frictional case. For both the contact area and mean contact pressure plots, fewer displacement increments were required for the frictionless simulations, leading to slightly smoother curves and minor differences in the representation of these local variations. Overall, the results show that friction had a limited influence on the contact interaction between the gripper fingers and the test object.

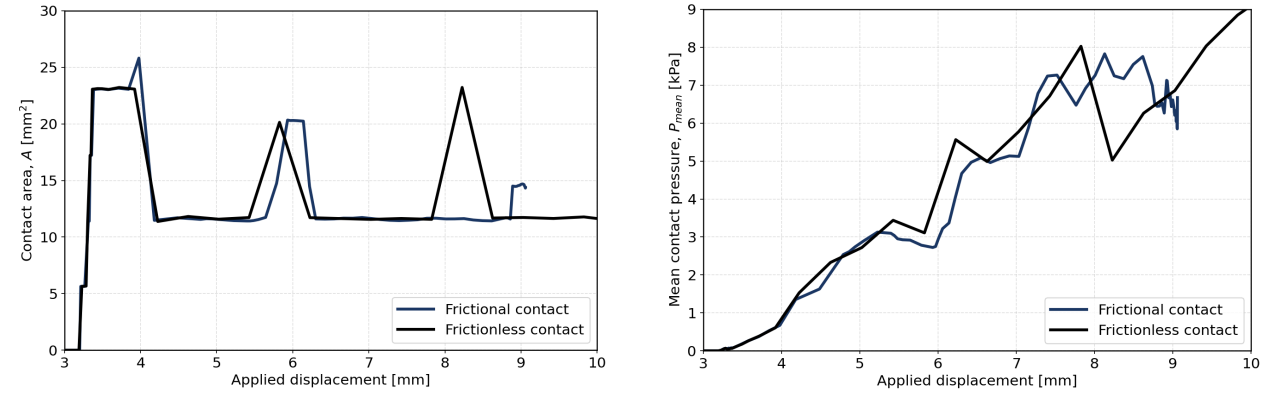

(a) (b)

Figure 28: Contact area and mean contact pressure versus applied displacement for a deformable test object under frictional and frictionless contact conditions.

5 Discussion

This thesis demonstrated that axial loading of a chiral mechanical metamaterial integrated into a soft robotic gripper leads to a rotational motion of the gripper. Furthermore, this rotational motion was successfully transferred to both rigid and deformable test objects through frictional contact between the gripper and the test object. In addition to the rotational response, the contact behavior between the gripper and the test object was evaluated under both frictional and frictionless contact conditions, providing insight into the contact behavior during twisting.

The results in Section 4.1 showed that the thickness, size, and orientation of the chiral column had the greatest influence on the rotational motion transferred to the gripper. For a thicker chiral column, the increased stiffness limits internal rotational deformation. However, the larger and stiffer ligaments enable more efficient transfer of axial deformation into rotational motion of the gripper. Increasing the unit cell size resulted in a larger rotational response, as axial compression produces larger lateral displacements in regions of the chiral structure located farther from the rotation axis. Rotating the chiral column by 45° increased the rotational response by aligning the gripper arms with the corners of the chiral column, which undergo the largest lateral displacements during axial compression.

An increase in the number of unit cells in the chiral column from two to four did not result in an improved rotational response of the gripper. The applied axial deformation was distributed over a greater length of the chiral column, reducing the internal twist of each unit cell and limiting the overall rotation transferred to the gripper. As larger applied displacements were evaluated for the final gripper design, the rotation angle reached a maximum at an applied displacement of approximately 12.5 mm and subsequently approached a constant value of about 12.68° for larger displacements. This behavior indicates that the chiral column reached a geometric limit, beyond which additional axial deformation could no longer be converted into rotational motion. This result is therefore an important consideration when defining the operating range of the actuator in the gripper design.

To evaluate the transfer of rotational motion to both rigid and deformable test objects, frictional contact was applied between the gripper and the test object. Under these contact conditions, the simulations involving a rigid test object exhibited limited numerical convergence, while the deformable test object showed improved convergence behavior. A rigid test object is not able to deform when in contact with the gripper, which leads to abrupt changes in the contact region during gripper rotation and makes numerical convergence more difficult. In contrast, a deformable object can adapt its shape during interaction with the gripper, leading to smoother contact evolution and improved convergence behavior. Over the displacement range for which the rigid-object simulation converged, the rigid and deformable test objects exhibited similar rotational behavior. This can be explained by the flexibility of the gripper, which allows the gripper fingers to deform around the test object during rotation. Therefore, the rotational response of the test object is mainly determined by the deformation of the gripper rather than by the stiffness of the test object.

A significant difference is observed between the rotation of the deformable test object and the rotation achieved by the gripper. The deformable test object achieved a rotation of 31.32° at an applied displacement of approximately 9 mm, and the gripper rotation reached a constant value of 12.68° at larger applied displacements. This difference arises because the gripper rotation was measured at the end of the gripper arms rather than at the tip of the gripper fingers. This location was chosen to provide a consistent measure of the global rotational behavior of the gripper for comparing different gripper designs. The rotation of the object results from the tangential motion of the gripper fingers along its surface, which experience a larger rotation due to the inward bending of the gripper fingers during twisting. As a result, the gripper rotation and object rotation represent different physical measures and cannot be directly compared.

Friction plays an important role in enabling the transfer of rotational motion to the test object. To evaluate whether friction influenced the contact between the gripper and the object, a frictionless case was introduced. Comparing the frictional and frictionless cases shows that the influence of friction on the contact behavior was limited, indicating that the contact behavior during twisting was largely determined by normal contact interactions. Over the converged displacement range, rigid and deformable test objects showed similar contact behavior for both frictional and frictionless cases. This indicates that object rigidity had a limited influence due to the flexibility of the gripper. For the deformable test object, continuous contact was maintained during twisting for both frictional and frictionless cases. The contact area approached a constant value with some temporary local peaks, while the mean contact pressure increased with applied displacement, with minor local variations. These local peaks occur as the gripper fingers slide along the test object, temporarily increasing the contact area at certain positions before returning to the steady contact value.

This thesis focused exclusively on numerical simulations without experimental validation of the gripper design due to the limited timeframe of a bachelor's project. As a result, an idealized smooth spherical test object was used, which does not fully represent the irregular shapes and surface properties of real agricultural products. Future work should therefore focus on experimental validation of the gripper design using real agricultural products. Furthermore, contact behavior was evaluated using the contact area and mean contact pressure, showing that continuous contact is maintained and that the interaction between the gripper and the object develops gradually during most of the twisting. These results provide insight into the contact interaction, but they do not alone determine whether the grasp is mechanically stable. Future work should therefore include additional contact metrics, such as pressure uniformity and variability, to better characterize grasp quality and evaluate whether the observed contact behavior indicates mechanical stability. In addition, the gripper frame geometry was not optimized in this thesis, as the focus was on the integration of the chiral metamaterial. The hollow frame resulted in a highly flexible structure with limited rigidity, which may limit its practical applicability. Future work could further investigate increasing the rigidity of the gripper frame, for example, by integrating internal metamaterial structures and evaluating how this influences the contact behavior.

6 Conclusion

Integrating a chiral mechanical metamaterial into a soft robotic gripper enables axial loading to be converted into controlled rotational motion of the gripper, which can be effectively transferred to grasped objects. This rotational transfer occurs while continuous contact is maintained during twisting for deformable objects intended to represent real agricultural products.

The results show that the rotational response of the gripper can be tuned through the geometry and orientation of the chiral structure. In addition, rotational motion of the gripper can be transferred to a grasped object through frictional contact. Over the converged displacement range, rigid and deformable test objects exhibit similar contact behavior, indicating that the interaction is largely determined by the flexibility of the gripper. A comparison of frictional and frictionless contact conditions shows that, while friction enables the transfer of rotational motion, the contact behavior during twisting remains similar for deformable objects.

Enabling gentle and continuous contact while introducing a controlled twisting motion of the grasped object demonstrates the potential of chiral mechanical metamaterials to enhance soft robotic grippers. This combined grasping and twisting capability may reduce the need for additional actuators and simplify the mechanical design of grippers for handling delicate agricultural products.

Bibliography

[1] J. F. Elfferich, D. Dodou, and C. Della Santina, "Soft grippers for crop handling and harvesting: State-of-the-art analysis," *Journal of Field Robotics*, vol. 10, pp. 75428–75443, 2022.

[2] S. Terrile, M. Argüelles, and A. Barrientos, "Comparison of different technologies for soft robotics grippers," *Sensors*, vol. 21, no. 3253, 2021.

[3] E. Navas, R. Fernández, D. Sepúlveda, M. Armada, and P. G. de Santos, "Soft grippers for automatic crop harvesting: A review," *Sensors*, vol. 21, no. 8, 2021.

[4] K. Bertoldi, V. Vitelli, J. Christensen, and M. van Hecke, "Flexible mechanical metamaterials," *Nature Reviews Materials*, vol. 2, no. 17066, 2017.

[5] H. Wang, Y. Lyu, S. Bosiakov, H. Zhu, and Y. Ren, "A review on the mechanical metamaterials and their applications in the field of biomedical engineering," *Frontiers in Materials*, vol. 10, no. 1273961, 2023.

[6] C. Tawk, R. Mutlu, and G. Alici, "A 3d printed modular soft gripper integrated with metamaterials for conformal grasping," *Frontiers in Robotics and AI*, vol. 8, no. 799230, 2022.

[7] S. D. Qin, Z. Y. Huang, W. D. Cao, X. F. Cao, and Y. S. Lin, "Dynamic compression mechanical behavior of three-dimensional chiral mechanical metamaterials: Effects of geometric parameters and size," *Materials*, vol. 18, no. 2584, 2025.

[8] K. K. Dudek, R. Gatt, K. W. Wojciechowski, and J. N. Grima, "Self-induced global rotation of chiral and other mechanical metamaterials," *International Journal of Solids and Structures*, vol. 191, pp. 212–219, 2020.

[9] J. Shintake, V. Cacucciolo, D. Floreano, and H. Shea, "Soft robotic grippers," *Advanced Materials*, vol. 30, no. 1707035, 2018.

[10] Y. Zhang, J. Man, X. Liu, S. Li, B. Cao, L. Yu, and X. Tan, "Soft robotic grippers: A review," *Frontiers in Materials*, vol. 12, no. 1692206, 2025.

[11] A. Kultongkham, S. Kumnon, T. Thintawornkul, and T. Chanthasopeephan, "The design of a force feedback soft gripper for tomato harvesting," *Journal of Agricultural Engineering*, vol. 52, no. 1, 2021.

[12] Y. Liu, L. Zhang, and X. Zhang, "Intelligent soft robotic grippers for agricultural and food applications," *Advanced Intelligent Systems*, vol. 5, 2023.

[13] A. Gunderman, J. Collins, A. Myers, R. Threlfall, and Y. Chen, "Tendon-driven soft robotic gripper for blackberry harvesting," *IEEE Robotics and Automation Letters*, vol. 7, pp. 2652–2659, 2022.

[14] Y. Zhao, X. Li, and L. Zhang, "Soft robotic grippers for agricultural applications: A review," *Machines*, vol. 13, no. 1, 2023.

[15] A. Ali, A. Mitra, and B. Aïssa, "Metamaterials and metasurfaces: A review from the perspectives of materials, mechanisms and advanced metadevices," *Nanomaterials*, vol. 12, no. 1027, 2022.

[16] X. Yu, J. Zhou, H. Liang, Z. Jiang, and L. Wu, "Mechanical metamaterials associated with stiffness, rigidity and compressibility: A brief review," *Progress in Materials Science*, vol. 94, pp. 114–173, May 2018.

[17] H. M. A. Kolken and A. A. Zadpoor, "Auxetic mechanical metamaterials," *RSC Advances*, vol. 7, pp. 5111–5129, 2017.

[18] J. ichiro Kishine, H. Kusunose, and H. M. Yamamoto, "On the definition of chirality and enantioselective fields," *Israel Journal of Chemistry*, vol. 62, 2022. Review article, Early Access October 2022.

[19] W. Wu, W. Hu, G. Qian, H. Liao, X. Xu, and F. Berto, "Mechanical design and multifunctional applications of chiral mechanical metamaterials: A review," *Materials & Design*, vol. 180, no. 107950, 2019. Review article.

[20] A. Alfonso, "Modulation of chiral metamaterials for biomedical implant applications," Jul. 2024.

[21] T. Frenzel, M. Kadic, and M. Wegener, "Three-dimensional mechanical metamaterials with a twist," *Science*, vol. 358, no. 6366, pp. 1072–1074, 2017.

[22] T. Frenzel, V. Hahn, P. Ziemke, J. L. G. Schneider, Y. Chen, P. Kiefer, P. Gumbsch, and M. Wegener, "Large characteristic lengths in 3d chiral elastic metamaterials," *Communications Materials*, vol. 2, no. 4, 2021.

[23] O. Igno, J. Rodríguez, and H. Martinez-Hernandez, "Tomato classification based on laser metrology and computer algorithms," *Proceedings of SPIE - The International Society for Optical Engineering*, vol. 8011, pp. 258–, 08 2011.

[24] S. Ansari, M. K. Gohil, Y. Maeda, and B. Bhattacharya, "A new auxetic structure-based hybrid gripper for harvesting tomato-like soft fruits," *International Journal of Intelligent Robotics and Applications*, 2025.

[25] I. Spanos, A. G. P. Kottapalli, and A. O. Krushynska, "Redefining grip: Quantitative evaluation of soft grippers with integrated metamaterials." Manuscript in preparation, 2025.

[26] R. Eusterbrock, "Development of a self-adaptive soft gripper for tomato handling and processing applications," 2024.

Appendices

This report has been produced in the framework of an educational program at the University of Groningen, Netherlands, Faculty of Science and Engineering, Industrial Engineering and Management (IEM) Curriculum. No rights may be claimed based on this report. Citations are only allowed with explicit reference to the status of the report as a product of a student project.

ChatGPT (OpenAI) was used to support the writing process of this report by assisting with language refinement, grammar, and clarity of expression. In addition, it was used to help identify potentially relevant scientific literature. All scientific reasoning, interpretation, technical content, modeling, analyses, and conclusions were carried out by the author.

Appendix A: CadQuery Scripts

A.1 : Chiral Column Generation Script

```
import cadquery as cq
from cadquery import Edge, Vector
import math

# Parameters
R1 = 19.224 # circle radius
thickring = 3.888# ring thickness
thickarm = 2.88 # arm thickness
delta = 34.8 # twist angle in degrees
e = 2.88 # extrusion thickness
a = 72 # size of the lattice constant
az = 2/3 *a # size of the unit cell

# Building ring
outer = cq.Workplane("XY").cylinder(e, R1)
inner = cq.Workplane("XY").cylinder(e, R1-thickring )
ring = outer.cut(inner)

# Building the left lower arm
corner = az/2
s = corner * math.tan(math.radians(delta))

# Computing the position of the end of the arm
x_end = -corner
y_end = -(corner + s)

# Y cannot go lower than -corner to stay inside the square face of the chiral column
if y_end < -corner:
    y_end = -corner

bottom_arm = (cq.Workplane("XY").polyline([(0.0, -R1),(0.0, -(R1 - thickarm)),(x_end, y_end + thickarm),(x_end, y_end)])
.close().extrude(e/2, both=True))

# Copy the left lower arm and rotate to get the other arms
arm2 = bottom_arm.rotate((0,0,0), (0,0,1), 90)
arm3 = bottom_arm.rotate((0,0,0), (0,0,1), 180)
```

```
arm4 = bottom_arm.rotate((0,0,0), (0,0,1), 270)

all_arms = bottom_arm.union(arm2).union(arm3).union(arm4)
face = ring.union(all_arms)

# Make cube of the chiral unit cell
bb = face.val().BoundingBox()
cx = (bb.xmin + bb.xmax) / 2
cy = (bb.ymin + bb.ymax) / 2
face = face.translate((-cx, -cy, 0))

# Place same face on each side of the cube
faces = []

# Making the 6 faces of the chiral unit cell
faces.append(face.translate((0,0,(az/2 - e/2))))
faces.append(face.rotate((0,0,0),(1,0,0),180).translate((0,0,-(az/2 - e/2))))
faces.append(face.rotate((0,0,0),(0,1,0),90).translate(((az/2 - e/2),0,0)))
faces.append(face.rotate((0,0,0),(0,1,0), -90).translate((-(az/2 - e/2),0,0)))
faces.append(face.rotate((0,0,0),(1,0,0), -90).translate((0,(az/2 - e/2),0)))
faces.append(face.rotate((0,0,0),(1,0,0),90).translate((0,-(az/2 - e/2),0)))

cube = faces[0]
for f in faces[1:]:
    cube = cube.union(f)

# Making a unit cell column
bb0 = cube.val().BoundingBox()
cube = cube.translate((0,0,-bb0.zmin))

# Stacking the columns
stack = cube.union(cube.translate((0,0,az)))
result = stack

# Show the chiral column
show_object(result)
```

A.2: Gripper and Chiral Column Assembly Script

```
import cadquery as cq

# Parameters
thickz = 10  # Frame thickness
tomatodia = 70  # Maximum object diameter
halfdia = tomatodia / 2
Depthgrip = tomatodia + 38  # Overall gripper depth

# Outer frame
outer_pts = [(halfdia,0),(50,20),(halfdia + 4,Depthgrip),(halfdia,Depthgrip),(
    halfdia,38),(-halfdia,38),(-halfdia,Depthgrip),(-halfdia-4,Depthgrip)
    ,(-50,20),(-halfdia,0)]

# outer U shape
outer2d = cq.Workplane("XY").polyline(outer_pts).close()
outer3d = outer2d.extrude(thickz)
```

```
15
16 # Cut out inner frame
17 inner_offset = 4.0
18 inner_pts = [(halfdia,0),(50,20),(halfdia+4,Depthgrip),(halfdia,Depthgrip),(
       halfdia,38),(-halfdia,38),(-halfdia,Depthgrip),(-halfdia-4,Depthgrip)
       ,(-50,20),(-halfdia,0)]
19 inner2d = cq.Workplane("XY").polyline(inner_pts).close().offset2D(-inner_offset)
20 inner3d = inner2d.extrude(thickz + 2)
21
22 # Final gripper frame
23 frame = outer3d.cut(inner3d)
24
25 # Cutting under bar
26 y_clear = 4.0
27 cutter = (cq.Workplane("XY").box(2*halfdia + 100, y_clear, thickz + 10, centered
       =(True, False, True)))
28 frame = frame.cut(cutter)
29
30 # Make 4 finger gripper
31 bb = frame.val().BoundingBox()
32 center_x = (bb.xmin + bb.xmax) / 2
33 center_y = (bb.ymin + bb.ymax) / 2
34 center_z = (bb.zmin + bb.zmax) / 2
35
36 # Rotate frame around own center
37 gripper_rotated = frame.rotate((center_x, center_y, center_z),
38 (center_x, center_y + 1, center_z),90)
39
40 # Make one gripper of 4 fingers
41 gripper_4finger = frame.union(gripper_rotated).clean()
42
43 # Import chiral column into script
44 from chiral72mm import result as chiral_column
45
46 # Finding the center of the chiral column-
47 bb_col = chiral_column.val().BoundingBox()
48 cx = (bb_col.xmin + bb_col.xmax) / 2
49 cy = (bb_col.ymin + bb_col.ymax) / 2
50 cz = (bb_col.zmin + bb_col.zmax) / 2
51
52 # Moving the column to the origin
53 column = chiral_column.translate((cx, cy, cz))
54
55 # Rotate around origin
56 column = column.rotate((0,0,0), (1,0,0), 270)
57
58 # 45 degrees rotation around y-axis
59 column = column.rotate((0,0,0), (0,1,0), 45)
60
61 # Translate the column into the correct position
62 column = column.translate((0, -110, 5))
63
64 # Add column to the gripper
65 gripper_with_chiral = gripper_4finger.union(column).clean()
66 # Plot gripper design
67 show_object(gripper_with_chiral)
```

Appendix B: MATLAB Script for Visualization of Rotation Results

```
clc; clear;
% This script loads rotation and displacement data exported from
% Abaqus and stored in Excel files, and generates plots of the
% rotation angle vs the applied displacement.

% Specify the Excel file and column names to be plotted
filename = 'example_data.xlsx';

displacement = {'Displacement_1_mm', 'Displacement_2_mm'};
angle        = {'Angle_1_deg', 'Angle_2_deg'};
legend     = {'Configuration 1', 'Configuration 2'};

% Read data
data = readtable(filename);

%Create figure
figure;
hold on;

for i = 1:length(displacement)
    plot(data.(displacement{i}), data.(angle{i}), 'o', ...
        'MarkerSize', 3, ...
        'LineStyle', 'none');
end

xlabel('Applied displacement [mm]', 'FontSize', 11);
ylabel('Rotation angle [deg]', 'FontSize', 11);
title('Rotation angle versus applied displacement', 'FontSize', 12)
   ;
legend(legendLabels, 'Location', 'northwest');

grid on;
box on;
set(gca, 'FontSize', 10);
hold off;
```

Appendix C: Python Scripts for Visualization of the Contact Behavior

C.1: Script for Exporting Contact Data from Abaqus

```python
from odbAccess import openOdb
import csv
import os

# Define the folder path containing the .odb files
folder_path = r"C:\Users\Tijnv"

odb_files = []
filename = "example.odb"
odb_files.append(filename)
target_surface = "test_object_surface"

for odb_filename in odb_files:
    odb_path = os.path.join(folder_path, odb_filename)

    # Check if the file exists before proceeding
    if not os.path.exists(odb_path):
        print(f"Warning: {odb_path} not found. Skipping...")
        continue

    # Open the ODB file
    odb = openOdb(path=odb_path)

    # Get the first step
    step_name = list(odb.steps.keys())[0]  # Get first step name
    step = odb.steps[step_name]

    # Initialize lists for CNAREA, CNORMF, CPRESS data, and node coordinates
    cnarea_data = []
    total_cnarea_data = []
    cnormf_data = []
    cpress_data = []
    node_data = []

    # Extract the specific instance "PART-2-1"
    instance_name = target_surface
    try:
        instance = odb.rootAssembly.instances[instance_name]  # Direct
            dictionary access
    except KeyError:
        print(f"Instance {instance_name} not found in the ODB.")
        continue

    # Extract and store node coordinates for the selected instance (including Z
        coordinate)
    print(f"Extracting nodes from instance {instance_name}")
    for node in instance.nodes:
        node_data.append((node.label, node.coordinates[0], node.coordinates[1],
            node.coordinates[2]))  # Node ID, X, Y, Z

    # Save node coordinates to CSV
    node_csv_filename = f"nodes_{odb_filename.replace('.odb', '')}.csv"
    node_csv_path = os.path.join(folder_path, node_csv_filename)
```

```
51
52      with open(node_csv_path, mode="w", newline="") as file:
53          writer = csv.writer(file)
54          writer.writerow(["Node ID", "X", "Y", "Z"])  # Header
55          writer.writerows(node_data)  # Write node coordinates
56
57      print(f"Node coordinates saved to {node_csv_path}")
58
59      # Loop through each frame to extract CNAREA, CNORMF, and CPRESS data
60      for frame in step.frames:
61          time = frame.frameValue  # Time of the frame
62
63          # Find CNAREA field output dynamically
64          cnarea_keys = [key for key in frame.fieldOutputs.keys() if "CNAREA" in
                key]
65          cnormf_keys = [key for key in frame.fieldOutputs.keys() if "CNORMF" in
                key]
66          cpress_keys = [key for key in frame.fieldOutputs.keys() if "CPRESS" in
                key]
67
68          # Process CNAREA data
69          if cnarea_keys:
70              cnarea_key = cnarea_keys[0]  # Use the first CNAREA-related key
71              cnarea_field = frame.fieldOutputs[cnarea_key]
72
73              # Convert the generator to a list
74              cnarea_values = list(cnarea_field.values)
75
76              # Initialize total CNAREA for the current frame
77              total_cnarea = 0
78
79              # Loop through values and filter by the correct instance name
80              for node in cnarea_values:
81                  if hasattr(node, "instance") and node.instance.name ==
                        target_surface:
82                      total_cnarea += node.data  # Sum CNAREA only for the target
                            surface
83                      cnarea_data.append((time, node.nodeLabel, node.instance.name
                            , node.data))
84
85              total_cnarea_data.append((time, total_cnarea))
86          else:
87              total_cnarea_data.append((time, 0))
88
89          # Process CNORMF data
90          if cnormf_keys:
91              cnormf_key = cnormf_keys[0]  # Use the first CNORMF-related key
92              cnormf_field = frame.fieldOutputs[cnormf_key]
93              cnormf_values = list(cnormf_field.values)
94              for force in cnormf_values:
95                  if force.instance.name == instance_name:  # Filter by specific
                        instance
96                      position = force.nodeLabel if hasattr(force, "nodeLabel")
                            else None
97                      magnitude = force.magnitude  # Magnitude of the normal
                            contact force
```

```
                    cnormf_data.append((time, position, force.instance.name,
                        magnitude))

        # Process CPRESS data
        if cpress_keys:
            cpress_key = cpress_keys[0]  # Use the first CPRESS-related key
            cpress_field = frame.fieldOutputs[cpress_key]
            cpress_values = list(cpress_field.values)
            for pressure in cpress_values:
                if pressure.instance.name == instance_name:  # Filter by
                    specific instance
                    position = pressure.nodeLabel if hasattr(pressure, "
                        nodeLabel") else None
                    magnitude = pressure.data  # Use .data for CPRESS
                    cpress_data.append((time, position, pressure.instance.name,
                        magnitude))

    # Define the output CSV file paths
    total_cnarea_csv_filename = f"CNAREA_tot_{odb_filename.replace('.odb', '')}.
        csv"
    total_cnarea_csv_path = os.path.join(folder_path, total_cnarea_csv_filename)

    cnarea_values_csv_filename = f"CNAREA_{odb_filename.replace('.odb', '')}.csv
        "
    cnarea_values_csv_path = os.path.join(folder_path,
        cnarea_values_csv_filename)

    cnormf_csv_filename = f"CNORMF_{odb_filename.replace('.odb', '')}.csv"
    cnormf_csv_path = os.path.join(folder_path, cnormf_csv_filename)

    cpress_csv_filename = f"CPRESS_{odb_filename.replace('.odb', '')}.csv"
    cpress_csv_path = os.path.join(folder_path, cpress_csv_filename)

    # Save total CNAREA data to CSV
    with open(total_cnarea_csv_path, mode="w", newline="") as file:
        writer = csv.writer(file)
        writer.writerow(["Time", "Total CNAREA"])  # Header
        writer.writerows(total_cnarea_data)  # Write total CNAREA data for each
            frame

    # Save CNAREA values to CSV (all CNAREA data)
    with open(cnarea_values_csv_path, mode="w", newline="") as file:
        writer = csv.writer(file)
        writer.writerow(["Time", "Node/Element ID", "Instance", "CNAREA
            Magnitude"])  # Header
        writer.writerows(cnarea_data)  # Write all CNAREA values

    # Save CNORMF data to CSV
    with open(cnormf_csv_path, mode="w", newline="") as file:
        writer = csv.writer(file)
        writer.writerow(["Time", "Node/Element ID", "Instance", "CNORMF
            Magnitude"])  # Header
        writer.writerows(cnormf_data)  # Write all CNORMF values

    # Save CPRESS data to CSV
    with open(cpress_csv_path, mode="w", newline="") as file:
        writer = csv.writer(file)
```

```
        writer.writerow(["Time", "Node/Element ID", "Instance", "CPRESS
            Magnitude"])  # Header
        writer.writerows(cpress_data)  # Write all CPRESS values

    print(f"Total CNAREA data saved to {total_cnarea_csv_path}")
    print(f"All CNAREA values saved to {cnarea_values_csv_path}")
    print(f"CNORMF data saved to {cnormf_csv_path}")
    print(f"CPRESS data saved to {cpress_csv_path}")
```

C.2: Script for Analyzing Contact Data

```
import csv
import numpy as np
import os
import pandas as pd

# Files
folder_path = r"C:\Users\Tijnv"

selected_files = [
    "case1",
    "case2"
]

# Displacement rate
DISP_RATE = 10.0  # mm/s

# Data storage
data_metrics = {
    name: {
        "time": [],
        "displacement": [],
        "contact_area": [],
        "pressure_time": [],
        "pressure_displacement": [],
        "max_pressure": [],
        "mean_pressure": [],
        "std_dev": [],
        "variation_coefficient": [],
        "uniformity_index": []
    }
    for name in selected_files
}

# Read CNAREA
for name in selected_files:
    csv_path = os.path.join(folder_path, f"CNAREA_tot_{name}.csv")

    times, areas = [], []
    with open(csv_path, mode="r") as file:
        reader = csv.reader(file)
        next(reader)
        for row in reader:
            t = float(row[0])
            a = float(row[1])
```

```
            times.append(t)
            areas.append(a)

    data_metrics[name]["time"] = times
    data_metrics[name]["displacement"] = [t * DISP_RATE for t in times]
    data_metrics[name]["contact_area"] = areas


# Read CPRESS
for name in selected_files:
    cpress_csv = os.path.join(folder_path, f"CPRESS_{name}.csv")

    time_pressure_map = {}
    with open(cpress_csv, mode="r") as file:
        reader = csv.reader(file)
        header = next(reader)
        time_idx = header.index("Time")
        pressure_idx = header.index("CPRESS Magnitude")

        for row in reader:
            try:
                t = float(row[time_idx])
                p = float(row[pressure_idx]) * 1000  # MPa to kPa
                time_pressure_map.setdefault(t, []).append(p)
            except ValueError:
                continue

    for t, pressures in sorted(time_pressure_map.items()):
        contact_pressures = [p for p in pressures if p > 0]

        max_p = max(pressures)
        mean_p = np.mean(contact_pressures) if contact_pressures else 0.0
        std_p = np.std(contact_pressures) if contact_pressures else 0.0
        coef_var = std_p / mean_p if mean_p > 0 else 0.0
        uniformity = mean_p / max_p if max_p > 0 else 0.0

        data_metrics[name]["pressure_time"].append(t)
        data_metrics[name]["pressure_displacement"].append(t * DISP_RATE)
        data_metrics[name]["max_pressure"].append(max_p)
        data_metrics[name]["mean_pressure"].append(mean_p)
        data_metrics[name]["std_dev"].append(std_p)
        data_metrics[name]["variation_coefficient"].append(coef_var)
        data_metrics[name]["uniformity_index"].append(uniformity)


# Export time data
rows = []

for name, m in data_metrics.items():
    n = min(
        len(m["pressure_displacement"]),
        len(m["contact_area"])
    )

    for i in range(n):
        rows.append({
            "Name": name,
```

```
            "Step": i + 1,
            "Displacement_mm": m["pressure_displacement"][i],
            "Contact_Area": m["contact_area"][i],
            "Max_Pressure_kPa": m["max_pressure"][i],
            "Mean_Pressure_kPa": m["mean_pressure"][i],
            "Std_Dev_kPa": m["std_dev"][i],
            "Variation_Coefficient": m["variation_coefficient"][i],
            "Uniformity_Index": m["uniformity_index"][i],
        })

df = pd.DataFrame(rows)

output_path = os.path.join(folder_path, "contact_metrics.csv")
df.to_csv(output_path, index=False)

print(df.groupby("Name")["Displacement_mm"].max())
```

C.3: Script for Plotting Contact Data

```
import pandas as pd
import matplotlib.pyplot as plt
import os

# Files
csv_path = r"C:\Users\Tijnv\contact_metrics.csv"
folder_path    = r"C:\Users\Tijnv"

# Case definitions
cases = {
    "case_1": {
        "label": "Case 1",
        "color": (),
        "linestyle": "-",
    },
    "case_2": {
        "label": "Case 2",
        "color": (),
        "linestyle": "--",
    }
}

# Load and combine data
dfs = []
for name, path in csv_files.items():
    df = pd.read_csv(path)
    df["Case"] = name
    dfs.append(df)

df = pd.concat(dfs, ignore_index=True)
df = df[df["Case"].isin(cases.keys())]
df = df.sort_values(["Case", "Displacement_mm"])

# Plot style
plt.rcParams.update({
    "font.size": 15,
```

```
    "axes.grid": True,
    "grid.linestyle": "--",
    "grid.alpha": 0.4,
})

# Contact area plot
fig, ax = plt.subplots(figsize=(9, 6))

for case, style in cases.items():
    sub = df[df["Case"] == case]
    ax.plot(
        sub["Displacement_mm"],
        sub["Contact_Area"],
        label=style["label"],
        color=style["color"],
        linewidth=3,
        linestyle=style["linestyle"],
    )

ax.set_xlabel("Applied displacement [mm]")
ax.set_ylabel(r"Contact area, $A$ [mm$^2$]")
ax.legend(loc="lower right", fontsize=15, framealpha=0.85)

fig.tight_layout()
fig.savefig(os.path.join(output_folder, "contact_area_comparison.pdf"), dpi=300)
plt.show()

# Mean pressure plot
fig, ax = plt.subplots(figsize=(9, 6))

for case, style in cases.items():
    sub = df[df["Case"] == case]
    ax.plot(
        sub["Displacement_mm"],
        sub["Mean_Pressure_kPa"],
        label=style["label"],
        color=style["color"],
        linewidth=3,
        linestyle=style["linestyle"],
    )

ax.set_xlabel("Applied displacement [mm]")
ax.set_ylabel(r"Mean contact pressure, $P_{mean}$ [kPa]")
ax.legend(loc="lower right", fontsize=15, framealpha=0.85)

fig.tight_layout()
fig.savefig(os.path.join(output_folder, "mean_pressure_comparison.pdf"), dpi
    =300)
plt.show()
```